Oxygen isotopic compositions of fresh rooftop micrometeorites from the Budel collection—Insights into the contemporary cosmic dust flux

Guido JONKER [1]*, Flore van MALDEGHEM [2], Matthias van GINNEKEN [3],
Lisa KRÄMER RUGGIU[2], and Steven GODERIS [2]

[1]Department of Earth Sciences, Faculty of Science, Vrije Universiteit Amsterdam, Amsterdam, The Netherlands
[2]Archaeology, Environmental Changes, and Geo-Chemistry, Vrije Universiteit Brussel, Brussels, Belgium
[3]Centre for Astrophysics and Planetary Science, School of Physical Sciences, University of Kent, Canterbury, UK

*Correspondence

Guido Jonker, Department of Earth Sciences, Faculty of Science, Vrije Universiteit Amsterdam, De Boelelaan 1085, Amsterdam 1081HV, The Netherlands.

Email: guidojonker.vua@gmail.com

Abstract–Cosmic dust particles originate from a wide variety of solar system and interstellar objects, including sources not identified among meteorite collections. Particles that survive atmospheric entry are retrieved on the Earth's surface as micrometeorites. The recovery of these micrometeorites has recently advanced to rooftop sites. Here, we present the results of an extensive isotopic study on this type of rooftop micrometeorite from the Budel collection, the Netherlands, accreted to the Earth between October 31, 2018 and June 16, 2021. The triple oxygen isotopic compositions of 80 silica-dominated cosmic spherules (CSs) with diameters ranging between 105 and 515 μm are obtained relying on 213 in situ spot analyses determined using ion microprobe. Our analyzed population spans a large range of isotopic compositions and is dominated by carbonaceous chondritic sources. In situ measurements on several CSs support a possible continuum between ^{16}O-rich and ^{16}O-poor compositions following the CM mixing line, showing that ^{16}O-poor CSs may be genetically related to aqueously altered carbonaceous chondrites. We demonstrate that weathering in the terrestrial environment has negligible effects on the isotopic compositions of the studied CSs and attempt to quantify the effects of kinetic mass-dependent fractionation and admixture of terrestrial oxygen during atmospheric entry. The results further corroborate previously suggested relations between CS texture and the duration and intensity of the heating pulse experienced during atmospheric deceleration. Finally, the young and well-constrained terrestrial age of the collection provides insights into the most recent flux of cosmic dust. Our results indicate no major recent changes in the global flux compared with collections sampled over thousand- to million-year time scales and demonstrate that ^{16}O-poor material is still represented in the modern-day cosmic dust flux at a relative abundance of ~13%–15%. As such, rooftop micrometeorites represent a valuable reservoir to study the characteristics of the contemporary cosmic dust flux.

INTRODUCTION

Micrometeorites are particles of extraterrestrial origin ~50–2000 μm in size collected on the Earth's surface (Genge et al., 2008; Taylor et al., 2016). During atmospheric entry, micrometeoroids decelerate and experience frictional heating. If peak temperatures remain sufficiently low, then micrometeorites may retain some of their preatmospheric textures and mineralogy, forming unmelted and partially melted scoriaceous micrometeorites, or relict-bearing spherules (Genge et al., 2008). Higher peak temperatures will result in melting and degassing, leading to

the formation of cosmic spherules (CSs; Love & Brownlee, 1991; Toppani et al., 2001). CSs are subdivided into several types according to their composition. Following the classification of Genge et al. (2008), these include the S-type (chondritic), I-type (Fe-dominated), and G-type (magnetite and silicate glass). According to their quench textures, S-type CSs are further subdivided into coarse-grained (CG), porphyritic olivine (PO), barred olivine (BO), cryptocrystalline (Cc), vitreous (V), and Ca-Al-Ti-rich (CAT) spherules (Brownlee et al., 1997; Taylor et al., 2000).

According to Love and Brownlee (1993), the Earth accretes roughly $30,000 \pm 20,000$ t of cosmic dust each year. However, flux estimates based on Antarctic micrometeorite collections indicate that each year only a few thousand tons of these particles accumulate on the Earth's surface (Rojas et al., 2021; Suttle & Folco, 2020; Taylor et al., 1998). These numbers imply that $\sim$50%–90% of the mass of cosmic dust particles entering the Earth's atmosphere breaks up and evaporates. Nonetheless, the micrometeorite flux to the Earth's surface is about two orders of magnitude larger than the meteorite flux (Bland et al., 1996). Cosmic dust particles sample a wide range of parental sources distinct from meteorites and thus provide additional means to study the diversity of solar system objects.

Meteorites record a large variation in isotopic compositions reflecting fundamental processes operating during the solar system's formation, including condensation and modification of a heterogeneous nebula, and later reprocessing by differentiation, brecciation, melting, aqueous alteration, and thermal metamorphism of agglomerated bodies (Franchi, 2008). Various major and trace elemental compositions and isotopic systems, including isotopes of O, Mg, Si, Fe, Cr, Ni, and K, are used to gain insights into these processes as well as the relationships between meteorites and micrometeorites and the effects of heating during atmospheric entry (e.g., Alexander et al., 2002; Brownlee et al., 1997; Cordier et al., 2011; Engrand et al., 2005; Herzog et al., 1999; Imae et al., 2013; Lampe et al., 2022; Rudraswami, Prasad, Babu, et al., 2016; Taylor et al., 2005).

Triple oxygen isotopic compositions of micrometeorites are reminiscent of their source material and can be used to explore the relationship with meteorite groups. Clayton et al. (1986) first used bulk oxygen isotope analyses on large numbers of CSs and concluded that, contrary to most meteorites, micrometeorites primarily show affinities with carbonaceous chondrites (CCs). Several subsequent studies have corroborated this finding (Cordier et al., 2011, 2012; Cordier & Folco, 2014; Engrand et al., 1999, 2005; Goderis et al., 2020; Gounelle et al., 2005; Lampe et al., 2022; Rudraswami et al., 2020; Rudraswami, Suttle, et al., 2022; Suavet et al., 2010; Taylor et al., 2005; van Maldeghem et al., 2023; Yada

et al., 2005), although a few studies indicated a significant contribution of ordinary chondrites (OC) among the larger size fractions (Suavet et al., 2011; Suttle et al., 2020; van Ginneken et al., 2017). The compiled results from these studies show that the relative contribution of OC parent bodies to the micrometeorite flux increases with particle size, from $\sim$7% below 500 μm to 38% above 500 μm (van Ginneken et al., 2017) and $\sim$70% above 800 μm (Suavet et al., 2011), indicating a gradual transition between CC-dominated micrometeorites and OC-dominated meteorites (Cordier & Folco, 2014). Particles >50 μm in size are commonly thought to be predominantly sourced from asteroids (Cordier & Folco, 2014). In contrast, some models suggest that Jupiter-family comets (JFCs) may be the main source of carbonaceous dust particles $\sim$10–1000 μm in size contributing to the zodiacal dust cloud (Nesvorný et al., 2010). The survival of these micrometeoroids upon entering the Earth's atmosphere is ensured by the generally low entry velocities resulting from Poynting–Robertson light drag.

Within the triple oxygen isotope diagram, Suavet et al. (2010) assigned micrometeorites to four distinct groups. Micrometeorites from groups 1 and 2 are genetically related to CCs with group 1 being attributed mainly to CO/CV chondrites and their refractory components, including Ca-Al-rich inclusions (CAIs), and group 2 to CM/CR chondrites. Group 3 correlates to OCs LL/L/H. Finally, group 4 is used to describe ^{16}O-poor micrometeorites that to date have not been observed among larger meteorite collections. The lack of a group 4 isotopic signature in meteorite collections could be caused by the friability of the parent body, which only produces small particles upon impact or causes the disintegration of the meteoroids during atmospheric entry (Matrajt et al., 2006).

Two main processes alter the primordial oxygen isotopic composition of cosmic dust particles during atmospheric entry heating (Clayton et al., 1986; Engrand et al., 2005; Rudraswami et al., 2020; Soens et al., 2022; Suavet et al., 2010; Taylor et al., 2005; Yada et al., 2005). A kinetic mass-dependent fractionation effect is caused by the preferential evaporation of ^{16}O because of its lower nuclide mass. As the micrometeoroid loses mass, this process enriches the particle in heavier isotopes, shifting values in a triple isotope plot to higher δ^{17}O and δ^{18}O parallel to the terrestrial fractionation line (TFL, defined as $\delta^{17}O = 0.52 \times \delta^{18}O$; Clayton, 1993). Simultaneously, the mixing of intrinsic oxygen with atmospheric oxygen brings values closer to the isotopic composition of the upper atmosphere. Hence, the variation of oxygen isotopes in CSs can be used as a proxy for the thermal reprocessing of micrometeoroids in the atmosphere.

Micrometeorites have frequently been recovered from Antarctic sites, deep-sea sediments, and hot deserts with a wide variety of terrestrial ages (Brase et al., 2021; Duprat et al., 2007; Genge et al., 2018; Goderis et al., 2020; Maurette et al., 1991; Prasad et al., 2013; Rudraswami, Parashar, et al., 2011; Taylor et al., 1998; van Ginneken et al., 2017; Yada et al., 2004). More recently, an abundance of CSs has been found in populated areas by sampling rooftop sites (Genge, Larsen, et al., 2016; Jonker, van Elsas, et al., 2023; Suttle, Hasse, et al., 2021). We present the results of the first extensive oxygen isotope study on a representative population of rooftop micrometeorites from the Budel collection (Jonker, van Elsas, et al., 2023), which represents the present-day micrometeorite flux. 80S-type CSs of all textural subtypes except CAT were analyzed for their triple oxygen isotopic composition based on 213 individual analyses using secondary ion mass spectrometry (SIMS). Previous isotope studies have often focused on large particles with diameters >250 μm. Few studies have primarily targeted smaller CSs (e.g., Rudraswami et al., 2020). The Budel collection, which consists mostly of CSs <300 μm in size, allows us to study these smaller size fractions. Within the collection, all major oxygen isotopic groups are represented. We demonstrate that the isotopic values have not been noticeably altered in the terrestrial environment and attempt to quantify the extent of oxygen evaporation and atmospheric mixing. Our findings corroborate previously suggested relations between CS texture, parentage, and degree of mass-dependent fractionation. Finally, the young and well-constrained terrestrial age of the rooftop micrometeorites in comparison with other collections provides insights into the most recent cosmic dust flux.

METHODS

Sample Selection

The micrometeorites analyzed in this study were obtained from the gutter of a large barn in Budel, the Netherlands (P. Beerten B.V.; 51°15′56.7″ N, 5°35′55.8″ E; constructed in 2006; Jonker, Schipper, et al., 2023). The roof has a total surface area of ~3600 m², of which ~3220 m² could be sampled. The CSs in this study are selected from the first of two sample batches collected on June 16, 2021 and May 15, 2022. The owners had previously emptied the gutter on October 31, 2018. The extraction of micrometeorites from the gutter samples involved the use of instruments from the Mineral Separation Laboratory (VU Amsterdam), including shape separation using a Faultable with an asymmetric vibrator and heavy liquid density separation using laboratory overflow centrifuges (Faul & Davis, 1959;

IJlst, 1973). A detailed description of the extraction methods is provided in Jonker, van Elsas, et al. (2023).

Micrometeorite identification was performed nondestructively with the JEOL Neoscope-II JCM-6000 benchtop scanning electron microscope (SEM) equipped with standardless energy-dispersive x-ray spectroscopy (EDS) at VU Amsterdam. The Budel collection consists of 1006 micrometeorites. One hundred fifteen spherules representing all CS textures except CAT were mounted in epoxy resin and polished, of which 80 were selected for oxygen isotope analysis (Table 1; Table S1). Average whole particle diameters were obtained from backscattered electron (BSE) images through a MATLAB code and range from 105 to 515 μm for the analyzed CSs, with most being <300 μm (Table 1; Jonker, Schipper, et al., 2023).

Rooftop micrometeorites are generally thought to be well-preserved due to young terrestrial ages compared to micrometeorites from most other collections (Genge, Larsen, et al., 2016, 2020; Suttle, Hasse, et al., 2021). Opposingly, the Budel micrometeorite collection contains several particles, especially V-type spherules, that display high degrees of alteration despite extremely short terrestrial residence times of <2.6 years (Jonker, van Elsas, et al., 2023). Sectioning of these particles has shown that this physical alteration is mostly superficial. For the oxygen isotope analyses, we deliberately selected six V-type spherules that display severe surface alteration resulting from weathering in the terrestrial environment to study the extent to which this alteration impacts the isotopic signatures.

Oxygen Isotope Measurements

The oxygen isotopic compositions of the CSs were measured in situ using the Cameca 1270 E7 secondary ion mass spectrometer at the Centre de Recherches Pétrographiques et Géochimiques (CRPG; Nancy, France). Oxygen ions ($^{16}O^-$, $^{17}O^-$, and $^{18}O^-$) were released from the sample by an incident Cs^+ primary ion beam (~15 μm spot size and ~2.5 nA beam current) and were simultaneously monitored in multicollection mode using two off-axis Faraday cups for $^{16}O^-$ and $^{18}O^-$ and the axial Faraday cup for $^{17}O^-$. Samples were probed for 275 s per spot including 90 s of presputtering. A mass resolving power of 2500 for $^{16}O^-$ and $^{18}O^-$ and 7000 for $^{17}O^-$ was applied to avoid $^{16}OH^-$ interference in the $^{17}O^-$ peak. Between two and six spots were analyzed per spherule.

Repeated analyses of several reference materials (San Carlos olivine, CLDR01, MORB glass, JV1 diopside, BHVO magmatic glass, Burma spinel, and Charoy magnetite) at the start and at the end of each session were used to define the instrumental mass fractionation line, to correct for instrumental mass fractionation due to matrix

TABLE 1. Size and average oxygen isotopic composition of different S-type cosmic spherules from coarse-grained to vitreous with possible parentage and group affinity.

Specimen	Type	Size (μm)	N	$\delta^{18}O$ (‰)	2SE	2SD	$\delta^{17}O$ (‰)	2SE	2SD	$\Delta^{17}O$ (‰)	2SE	2SD	Parent body	Group
GMM71	CG	297	4	5.25	0.6	14.4	−2.59	0.8	9.1	−5.32	0.8	1.7	CC	1
GMM87	CG	279	2	13.93	0.4	39.3	3.07	0.5	33.0	−4.17	0.5	12.5	CC/^{16}O-poor	Ambiguous
GMM112	CG	197	3	5.70	0.8	22.9	−0.48	0.7	10.9	−3.44	0.8	1.4	CC	Ambiguous
GMM118	CG	251	6	0.84	0.7	10.7	−2.90	0.9	5.7	−3.34	1.0	1.4	CC	Ambiguous
GMM137	CG	204	2	1.67	0.6	17.9	−4.26	0.5	10.9	−5.13	0.6	1.5	CC	1
GMM245	CG	145	3	5.81	0.8	3.9	3.53	1.0	0.9	0.51	1.0	2.1	OC/EC	3
GMM318	CG	172	3	5.34	0.8	4.6	−0.63	0.9	1.8	−3.41	1.0	0.6	CC	1
GMM409	CG	155	2	8.13	0.6	0.7	4.28	0.8	0.8	0.05	0.8	0.4	CC/OC/EC/ Ach	3
GMM415	CG	167	3	14.78	0.8	2.0	6.90	1.0	0.9	−0.78	1.0	0.5	CC	2
GMM424	CG	145	3	3.01	0.8	10.6	−0.11	1.0	5.3	−1.67	1.1	0.2	CC	2
GMM451	CG	137	4	4.91	1.0	4.7	−1.55	1.1	2.7	−4.10	1.2	0.5	CC	1
GMM483	CG	112	3	6.98	0.8	7.3	4.12	1.0	3.7	0.48	1.1	0.2	OC/EC	3
GMM4	PO	222	2	17.59	0.6	0.9	8.44	0.5	0.8	−0.71	0.6	0.3	CC	2
GMM7	PO[a]	202	4	19.12	0.8	17.7	6.29	0.7	11.2	−3.65	0.8	2.0	CC	1
GMM38	PO[a]	203	3	9.49	0.8	0.9	1.18	0.7	1.0	−3.75	0.9	0.9	CC	1
GMM59	PO[a]	300	3	21.10	0.8	23.4	10.54	0.7	14.7	−0.43	0.8	2.5	CC/^{16}O-poor	Ambiguous
GMM69	PO[a]	261	4	14.61	0.8	14.0	6.28	0.8	6.6	−1.31	0.9	1.0	CC	2
GMM80	PO[a]	300	5	0.78	0.7	34.8	−6.18	0.9	31.3	−6.59	1.0	13.5	CC/CAI	1
GMM92	PO[a]	212	3	4.83	0.9	10.9	−0.35	0.7	5.2	−2.86	0.9	0.6	CC	Ambiguous
GMM102	PO[a]	243	3	7.01	0.5	4.9	4.13	0.6	2.6	0.49	0.7	0.3	OC/EC	3
GMM110	PO	235	2	8.80	0.5	2.2	3.61	0.5	1.5	−0.96	0.6	0.3	CC	2
GMM113	PO[a]	208	3	8.56	0.7	2.7	2.28	0.6	1.3	−2.17	0.7	0.7	CC	2
GMM120	PO	208	2	6.37	0.5	2.4	−1.79	0.5	0.9	−5.10	0.6	0.4	CC	1
GMM148	PO[a]	199	4	5.05	0.8	23.3	−1.52	0.7	14.7	−4.14	0.8	2.6	CC	1
GMM173	PO[a]	222	3	12.99	0.7	38.7	3.41	0.7	23.1	−3.34	0.7	3.0	CC	1
GMM208	PO[a]	197	4	4.58	0.8	10.0	−2.18	0.7	5.6	−4.56	0.8	0.5	CC	1
GMM216	PO[a]	185	3	18.61	0.7	1.1	6.27	0.6	0.3	−3.41	0.7	0.5	CC	1
GMM217	PO	186	2	21.22	0.5	1.8	9.69	0.5	2.2	−1.35	0.5	1.3	CC	2
GMM218	PO[a]	234	5	11.74	0.9	21.2	2.26	0.8	12.9	−3.85	1.0	1.9	CC	1
GMM231	PO	243	2	7.88	0.4	0.1	4.22	0.5	0.4	0.12	0.6	0.4	OC/EC	3
GMM443	PO	156	3	35.74	0.8	2.7	20.75	1.0	1.5	2.17	1.0	0.2	^{16}O-poor	4
GMM75	PO-c[a]	294	3	37.14	0.5	3.0	20.38	0.6	1.3	1.07	0.7	0.3	^{16}O-poor	4
GMM136	PO-c[a]	194	3	26.31	0.8	10.5	15.07	0.7	6.2	1.39	0.8	1.1	^{16}O-poor	4
GMM422	PO-c	148	3	42.28	0.8	1.3	23.88	1.0	0.9	1.90	1.0	0.3	^{16}O-poor	4
GMM592	PO-c[a]	108	4	31.56	0.9	3.0	16.06	1.1	1.9	−0.36	1.2	0.9	CC/^{16}O-poor	Ambiguous
GMM629	μPO-c[a]	106	2	26.06	0.7	0.7	11.16	0.8	0.3	−2.39	0.9	0.7	CC	1
GMM128	μPo	186	2	17.79	0.6	0.9	5.74	0.6	0.8	−3.51	0.6	0.3	CC	1
GMM129	μPo[a]	183	3	20.78	0.9	4.3	7.05	0.7	3.6	−3.76	0.9	1.6	CC	1
GMM398	μPo[a]	138	3	23.95	0.8	4.6	10.46	1.0	2.6	−1.99	1.0	0.3	CC	Ambiguous
GMM633	μPo[a]	116	3	7.83	0.8	8.1	1.74	1.0	6.8	−2.33	1.0	4.8	CC	Ambiguous
GMM46	BO	400	2	19.44	0.4	0.3	7.51	0.5	0.1	−2.59	0.5	0.3	CC	1
GMM52	BO	288	2	31.74	0.4	1.0	17.10	0.5	1.4	0.60	0.5	0.9	^{16}O-poor	4
GMM61	BO	282	2	30.24	0.4	3.6	12.74	0.5	2.6	−2.98	0.5	0.7	CC	1
GMM66	BO	284	2	29.89	0.4	0.4	12.48	0.5	0.5	−3.06	0.5	0.3	CC	1
GMM67	BO	287	2	28.55	0.4	1.5	11.95	0.5	0.4	−2.90	0.5	0.3	CC	1
GMM140	BO	203	2	25.69	0.5	0.2	12.77	0.5	0.4	−0.59	0.5	0.5	CC	2
GMM160	BO	197	2	22.20	0.5	0.0	7.94	0.5	0.5	−3.60	0.5	0.5	CC	1
GMM171	BO	228	2	26.44	0.5	2.0	11.25	0.5	0.8	−2.50	0.6	0.2	CC	1
GMM172	BO	235	2	6.65	0.5	1.3	−0.51	0.5	0.6	−3.97	0.5	0.1	CC	1
GMM177	BO	248	2	22.10	0.4	0.7	7.23	0.5	0.9	−4.26	0.5	0.5	CC	1
GMM182	BO	206	2	31.75	0.5	2.2	14.29	0.5	1.4	−2.22	0.5	0.2	CC	1

TABLE 1. *Continued.* Size and average oxygen isotopic composition of different S-type cosmic spherules from coarse-grained to vitreous with possible parentage and group affinity.

Specimen	Type	Size (μm)	N	$\delta^{18}O$ (‰)	2SE	2SD	$\delta^{17}O$ (‰)	2SE	2SD	$\Delta^{17}O$ (‰)	2SE	2SD	Parent body	Group
GMM185	BO	239	2	29.74	0.4	1.7	12.26	0.5	0.6	−3.21	0.6	0.3	CC	1
GMM225	BO	246	2	44.31	0.4	2.3	24.87	0.5	0.6	1.82	0.5	0.6	^{16}O-poor	4
GMM37	Cc-m	297	2	28.56	0.4	5.5	12.55	0.5	3.9	−2.31	0.5	1.1	CC	1
GMM50	Cc-m	298	2	30.53	0.4	8.1	13.50	0.5	4.1	−2.38	0.5	0.1	CC	1
GMM53	Cc-m	319	2	18.95	0.4	8.2	7.18	0.5	3.9	−2.67	0.5	0.4	CC	1
GMM68	Cc-m	302	2	11.03	0.4	0.2	6.45	0.5	0.3	0.71	0.5	0.4	OC/EC	3
GMM122	Cc-m	203	2	8.50	0.5	1.1	1.12	0.5	0.9	−3.30	0.6	0.3	CC	Ambiguous
GMM36	Cc-n	279	2	35.44	0.4	1.4	18.69	0.5	0.6	0.26	0.5	0.0	^{16}O-poor	4
GMM44	Cc-n	515	2	11.82	0.4	2.4	4.12	0.5	0.7	−2.03	0.6	0.5	CC	2
GMM48	Cc-n	400	2	22.22	0.4	2.6	7.12	0.6	1.6	−4.44	0.6	0.2	CC	1
GMM115	Cc-n	225	2	3.22	0.5	0.3	−1.41	0.5	0.4	−3.08	0.5	0.3	CC	Ambiguous
GMM127	Cc-n	225	2	12.80	0.5	13.2	7.25	0.6	6.1	0.60	0.6	0.7	OC/EC	3
GMM64	Cc-t	283	2	32.29	0.4	1.6	12.88	0.5	0.7	−3.91	0.5	0.1	CC	1
GMM98	Cc-t	190	1	0.64	0.4	N/A	−0.89	0.5	N/A	−1.23	0.5	N/A	CC	2
GMM105	Cc-t	213	3	13.63	0.6	1.7	7.47	0.6	1.0	0.38	0.7	0.4	OC/EC	3
GMM117	Cc-t	206	2	18.86	0.5	1.4	9.40	0.4	0.3	−0.4	0.5	0.4	CC	2
GMM161	Cc-t	208	2	31.62	0.5	0.8	13.34	0.5	0.9	−3.1	0.6	0.5	CC	1
GMM397	Cc-t	150	3	28.06	0.8	0.6	13.82	1.0	0.3	−0.77	1.1	0.1	CC	2
GMM49	V	406	3	9.18	0.5	0.6	5.22	0.6	0.3	0.45	0.7	0.1	OC/EC	3
GMM84	V	308	3	5.99	0.5	2.3	2.72	0.7	0.7	−0.39	0.8	0.7	CC/OC/EC/ HED	Ambiguous
GMM85	V	317	2	8.26	0.4	2.0	4.90	0.5	1.1	0.60	0.5	0.1	OC/EC	3
GMM109	V[b]	253	3	37.09	0.5	5.3	17.97	0.7	3.3	−1.32	0.7	0.6	CC	1
GMM114	V[b]	201	2	37.18	0.5	1.4	16.55	0.5	0.9	−2.78	0.5	0.2	CC	1
GMM116	V[b]	218	3	39.90	0.7	6.4	18.65	0.6	3.3	−2.10	0.7	0.4	CC	1
GMM233	V[b]	207	3	24.36	0.7	1.1	11.79	0.6	0.6	−0.87	0.7	0.5	CC	2
GMM234	V[b]	203	2	53.65	0.5	2.9	29.24	0.5	0.7	1.35	0.6	0.8	^{16}O-poor	4
GMM414	V	146	3	45.94	0.8	0.7	25.64	1.0	0.4	1.76	1.0	0.3	^{16}O-poor	4
GMM429	V[b]	158	3	50.12	0.8	2.9	27.81	0.9	1.3	1.75	1.0	0.3	^{16}O-poor	4
GMM648	V	112	3	32.22	0.8	2.7	15.95	1.0	1.1	−0.80	1.0	0.7	CC	2

Note: Isotopic values are given in permil (‰) relative to V-SMOW; given sizes are average diameters of the spherules. Textural type: CG, coarse-grained (S-type); BO, barred olivine; Cc, cryptocrystalline (−m, microcrystalline; −n, normal; −t, turtleback); PO, porphyritic olivine (μ, microporphyritic; −c, cumulate); V, vitreous. Precursor affinity: Ach, achondrite; CC, carbonaceous chondrite; EC, enstatite chondrite; HED, howardite/eucrite/diogenite-like; OC, ordinary chondrite. 2SE represents propagated analytical errors; 2SD represents the internal variation. Large 2SD is the result of internal heterogeneity, commonly associated with the presence of relicts. Each spherule is affiliated with possible precursors and isotopic groups taking into account particle heterogeneity, relict minerals, analytical uncertainties, and atmospheric entry effects. Ambiguous spherules cannot be assigned to an isotopic group with certainty.

[a]Relict-bearing porphyritic olivine spherule.

[b]Vitreous spherule with weathering characteristics.

effects, and to check the reproducibility of the data. The analytical 2 standard error (2SE) of in situ measurements during these sessions was determined to be ∼0.4–0.5‰ for $\delta^{18}O$ and ∼0.4–0.6‰ for $\delta^{17}O$ and $\Delta^{17}O$. The results are expressed in permil (‰) using standard δ notation relative to Vienna Standard Mean Ocean Water (V-SMOW) as $\delta^{18}O = [(^{18}O/^{16}O)_{sample}/(^{18}O/^{16}O)_{V\text{-}SMOW} − 1] \times 1000$ (‰), and using $^{17}O/^{16}O$ for $\delta^{17}O$. The deviation from the TFL is expressed as $\Delta^{17}O = \delta^{17}O − 0.52 \times \delta^{18}O$ (Clayton, 1993; Criss & Farquhar, 2008). In situ data are provided in Table S1. Averaged values for the analyzed spherules with 2 standard deviation (2SD) and propagated 2SE are reported in Table 1. The 2SD values represent the repeatability of multiple analyses on the same particle and are in some cases considerably larger than the 2SE as a result of the internal heterogeneity of these particles, commonly related to the presence of relict minerals. Uncertainties reported in the text are 2SE unless specified otherwise.
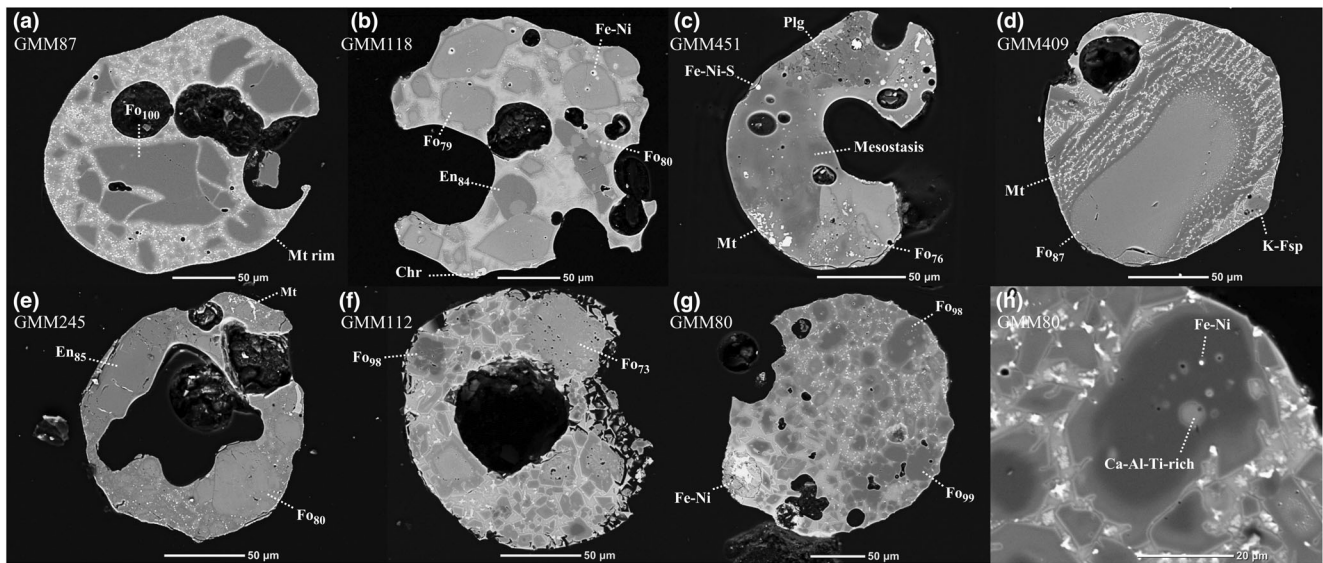
FIGURE 1. Polished-section backscattered electron images of representative CG-type and relict-bearing PO-type spherules with relict minerals that survived atmospheric entry. (a) Large partially melted forsterite relicts surrounded by matrix; fractures in the forsterite relicts point to shock fragmentation by a large thermal gradient, indicating the presence of preatmospheric hydrated phyllosilicates in the matrix. (b) Euhedral Fe-rich olivine and orthopyroxene relicts and a small chromite crystal; small anhedral olivines enclosed by orthopyroxenes may point to multiple crystal growth generations. (c) Partially melted plagioclase and Fe-rich olivine relicts and several Fe-Ni-S droplets; light-colored mesostasis is similar in composition to the olivine, while dark-colored mesostasis is similar to the plagioclase with enrichment of sodium. (d) Large partially melted Fe-rich olivine relict with several distinct concentric zones of magnetite formed by interaction with oxygen in the atmosphere; a K-rich feldspar sits in the bottom-right corner. (e) Fe-rich olivine and orthopyroxene relicts surrounding a large inner void. (f) Adjacent Mg-rich and Fe-rich olivine relicts with secondary growth; the latter are comparatively vesiculated. (g) PO-type spherule with several Mg-rich olivine relicts and a ring of beads at the exterior, of which one is visible in the section. (h) Detail of GMM80 exhibiting globules rich in calcium, aluminum, and titanium poikilitically enclosed in an olivine relict; combined with the ^{16}O-rich composition, they indicate a genetic relation to CAIs in carbonaceous chondrites.

RESULTS

Petrography

All CSs analyzed in this study (Table 1) were classified following the classification system proposed by Genge et al. (2008). Figures 1 and 2 show representative examples of the various textural types, which include CG ($n = 12$), PO ($n = 28$), BO ($n = 13$), Cc ($n = 16$), and V ($n = 11$). The Cc-type is further subdivided into three textural groups: microcrystalline ($n = 5$), normal ($n = 5$), and turtleback ($n = 6$) following Suttle and Folco (2020). We also differentiate two distinct textures among PO-types, differing from the regular PO texture: microporphyritic (μPO; $n = 5$) with small (less than a few μm) anhedral crystals and cumulate (PO-c; $n = 5$). One spherule displayed a combination of both textures. These textures have been suggested to reflect sources distinct from regular PO-type spherules (Genge, Suttle, et al., 2016; van Ginneken et al., 2017). An additional rb- (relict-bearing) prefix is used for PO-type spherules to indicate the presence of relict minerals that survived melting in the atmosphere ($n = 19$).

Relict anhydrous phases frequently encountered in the analyzed CSs (Figure 1) include Mg-rich olivine (Fo_{95-100}), Fe-rich olivine (Fo_{67-94}), and Mg-rich orthopyroxene (En_{84-96}). Additionally, rarer relict phases include chromite, Fe-Ni metal droplets enclosed in relict minerals, and refractory inclusions poikilitically enclosed in forsterite (GMM80; Figure 1h). GMM451 (Figure 1c) consists predominantly of partially melted relict plagioclase feldspar with minor Fe-rich olivine. GMM409 (Figure 1d) contains an enigmatic potassium-rich feldspar. Mg-rich olivine, Fe-rich olivine, orthopyroxene, and plagioclase relicts were in some cases sufficiently large ($>20\,\mu$m) to be analyzed for their oxygen isotopic composition without interference from surrounding phases.

Oxygen Isotopic Compositions

In total, 80 CSs were analyzed by 213 in situ measurements. Individual analyses are shown in Figure 3 and available in Table S1. Averaged isotopic compositions are summarized in Table 1 and Figure 4. The isotopic
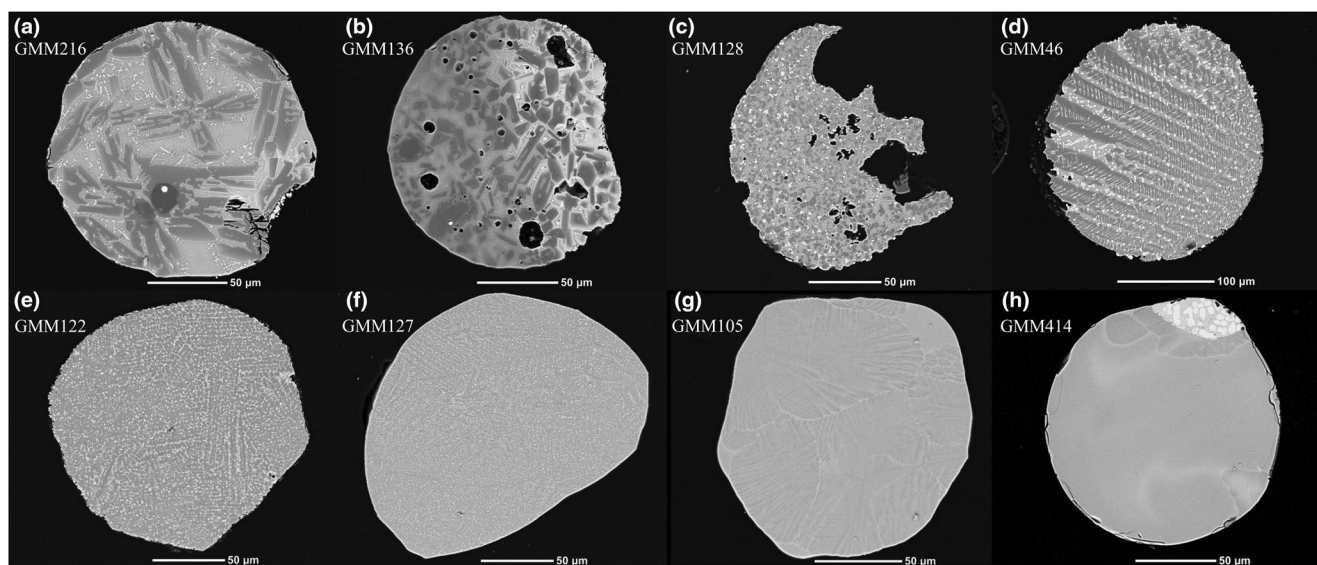
FIGURE 2. Polished-section backscattered electron images of representative examples of various types of CSs. (a) Normal PO-type with skeletal olivine crystals and a small forsterite relict with a Fe-Ni droplet. (b) PO-type with a cumulate texture. (c) PO-type with a microporphyritic texture consisting of small equidimensional crystals. (d) BO-type. (e) Cc-type with microcrystalline texture. (f) Cc-type with normal texture. (g) Cc-type with turtleback texture and morphology. (h) V-type with partial crystallization around a Fe-Ni-S bead; the bead displays segregation of S-rich (dark) and S-poor (light) phases.

compositions are commonly heterogeneous in CG- and PO-type spherules due to the presence of relict phases, while mostly homogeneous in BO-, Cc-, and V-type spherules that experienced complete melting and subsequent homogenization. The average $\delta^{18}O$ for all CSs increases as CG < PO < Cc < BO < V with respective values of 6.4 ± 8.5‰, 16.8 ± 21.8‰, 19.3 ± 21.9‰, 26.8 ± 17.3‰, and 31.3 ± 34.2‰ (2SD). The average $\Delta^{17}O$ increases as CG < BO < PO < Cc < V with respective values of −2.5 ± 4.3‰, −2.3 ± 3.6‰, −2.0 ± 4.5‰, −1.7 ± 3.4‰, and 0.6 ± 3.1‰ (2SD). The highest isotopic value is recorded in a V-type spherule with $\delta^{18}O = 54.7 ± 0.4$‰, $\delta^{17}O = 29.5 ± 0.4$‰, and $\Delta^{17} = 1.1 + 0.4$‰ (GMM234; Figure 3). The lowest isotopic value was measured in a rb-PO-type spherule with $\delta^{18}O = −27.7 ± 0.4$‰, $\delta^{17}O = −32.9 ± 0.5$‰, and $\Delta^{17}O = −18.5 ± 0.5$‰ (GMM80; Figure 3).

Relict minerals that were large enough (>20 μm) to be measured without interference from adjacent recrystallized phases plot mostly on or close to the Primitive Chondrule Minerals (PCMs) line with slope 0.987 (Ushikubo et al., 2012) and the Carbonaceous Chondrite Anhydrous Mineral (CCAM) line with slope ~0.94 (Clayton & Mayeda, 1977, 1999), or near the OC LL/L/H fields (Figures 3 and 5). For these relict minerals, the collective ranges of isotopic compositions are $\delta^{18}O$ from −6.4 ± 0.4‰ to 15.4 ± 0.5‰, $\delta^{17}O$ from −8.6 ± 0.4‰ to 7.3 ± 0.5‰, and $\Delta^{17}O$ from −8.6 ± 0.4‰ to 1.5 ± 0.5‰. The analyzed relicts include

eight Mg-rich olivines (Fo_{96-99}), 13 Fe-rich olivines (Fo_{73-91}), three orthopyroxenes (En_{84-85}), and a single plagioclase (An_{64}), deriving from 15 different CSs. For Mg-rich olivines, $\delta^{18}O$ ranges from −4.7 ± 0.4‰ to 15.4 ± 0.5‰, $\delta^{17}O$ from −8.6 ± 0.4‰ to 6.9 ± 0.6‰, and $\Delta^{17}O$ from −8.6 ± 0.4‰ to −0.6 ± 0.6‰. Ranges of Fe-rich olivines are comparable to those of Mg-rich olivines, with $\delta^{18}O$ from −6.4 ± 0.4‰ to 15.3 ± 0.5‰, $\delta^{17}O$ from −6.4 ± 0.4‰ to 7.3 ± 0.5‰, and $\Delta^{17}O$ from −3.7 ± 0.4‰ to 0.5 ± 0.4‰. Within the three orthopyroxene grains, $\delta^{18}O$ ranges from −5.4 ± 0.3‰ to 3.6 ± 0.4‰, $\delta^{17}O$ from −6.3 ± 0.4‰ to 3.4 ± 0.6‰, and $\Delta^{17}O$ from −4.0 ± 0.4‰ to 1.5 ± 0.6‰. The plagioclase relict yields values of $\delta^{18}O = 5.4 ± 0.5$‰, $\delta^{17}O = −1.1 ± 0.5$‰, and $\Delta^{17}O = −3.9 ± 0.6$‰.

To study the effect of weathering in the terrestrial environment on rooftop micrometeorites and the extent to which oxygen isotopic compositions may be altered, we deliberately selected six V-type spherules that displayed pronounced surface alteration (Jonker, van Elsas, et al., 2023). Following the weathering scale of van Ginneken et al. (2016), these can be assigned to the 1b to 2c scales, partial to complete encrustation with minor to moderate loss of primary material. Analyses near the weathered rim of these spherules show $\delta^{18}O$ values that differ from core values by 0.0‰ to −3.3‰. The remaining pristine V-type spherules show differences between rim and core values of +1.8‰ to +0.2‰, and cryptocrystalline domains differ from glassy domains by
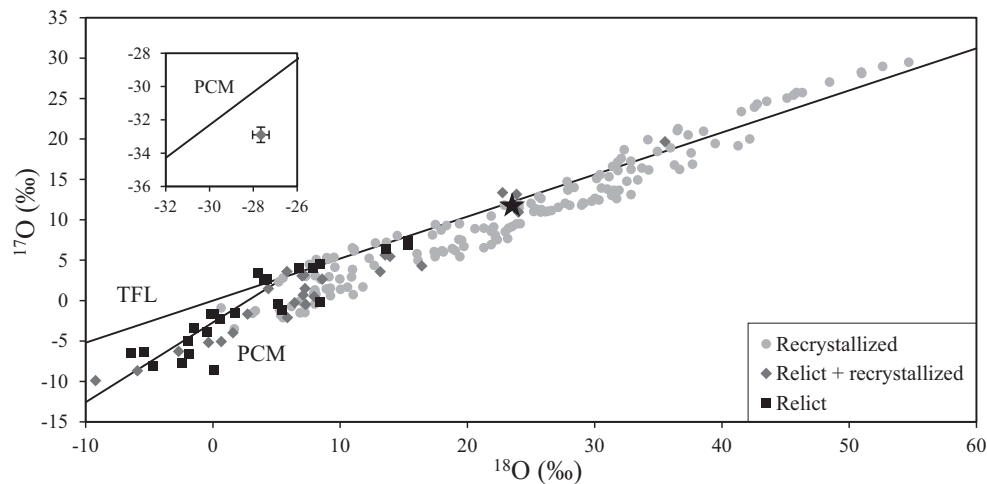
FIGURE 3. Plot of $\delta^{18}O$ versus $\delta^{17}O$ of 213 in situ analyses on relict minerals and recrystallized phases within 80 CSs of various textural types. Relict minerals plot near the PCM line with slope ~0.987 (Ushikubo et al., 2012). Recrystallized phases, including crystals and mesostasis, plot around the TFL with slope 0.52 (Clayton, 1993). The composition of atmospheric oxygen is represented by an asterisk ($\delta^{18}O = 23.5‰$, $\delta^{17}O = 11.8‰$; Thiemens et al., 1995). The inset shows a single measurement on GMM80 with an extremely ^{16}O-rich composition associated with Ca-Al-inclusions. 2SE analytical uncertainties on the data points are generally smaller than the symbols.

+2.6‰ to −5.9‰ in $\delta^{18}O$. Note that the analytical error on the data is up to ±0.5‰, thus the difference between two data points has an uncertainty of up to ±1.0‰.

DISCUSSION

Parent Body Affinities of Budel CSs

Major Isotopic Groups

Within the triple isotope plot shown in Figure 4b, the analyzed micrometeorites are clustered in isotopic groups previously defined by Suavet et al. (2010), who reported an apparent relation of spherules of group 1 to CO/CV chondrites, group 2 to CM/CR chondrites, group 3 to LL/L/H OCs, and group 4 to an unknown ^{16}O-poor source.

Our analyzed population includes CG- and PO-type spherules which have experienced limited isotopic alteration in the atmosphere, as well as V-type spherules that experienced strong isotopic alteration. In comparison, Suavet et al. (2010) based their isotopic groups mostly on comparatively large (>500 μm) BO-type and a few PO- and V-type spherules (Figure 4b). As a result, our data extend the ranges of the major isotopic groups. The individual spherule affinities and group allocations are reported in Table 1.

Group 1 CSs occur in a relatively narrow band with $\Delta^{17}O$ roughly between −3.5‰ and −5.5‰ at $\delta^{18}O \approx 0‰$, increasing to between −1‰ and −3‰ at $\delta^{18}O \approx 40‰$. Group 2 CSs plot between about −0.5‰ and −2‰ for $\Delta^{17}O$ with $\delta^{18}O$ between 0‰ and 35‰. Groups 1 and 2

thus appear to overlap in part, and a few spherules plot between these two groups. CSs belonging to group 3 plot around the TFL and above the atmospheric value within analytical uncertainty with $\Delta^{17}O$ between 0.0‰ and 0.8‰, and $\delta^{18}O$ between 5‰ and 15‰. Group 4 ^{16}O-poor spherules with $\Delta^{17}O$ above the atmospheric value describe a comparatively large isotopic range with $\Delta^{17}O$ between ~0.2‰ and ~2.2‰, and $\delta^{18}O$ between 25‰ and 55‰. Note that our results are based on averaged spot analyses and may thus not be fully representative of bulk spherule values.

Following these extended group definitions, approximately 43.8% ($n = 35$) of the analyzed spherules belong to group 1, 17.5% ($n = 14$) to group 2, 12.5% ($n = 10$) to group 3, and 12.5% ($n = 10$) to group 4. 13.8% ($n = 11$) of the spherules are ambiguous and cannot be affiliated to a specific group when analytical uncertainties, internal heterogeneity, and atmospheric entry effects are considered. Most of the ambiguous spherules plot within or between groups 1 and 2. Despite these outlier data points, the existence of these groups is still justified by the distribution of various CS types, for example, 10 out of 13 of the analyzed BO-type spherules plot below $\Delta^{17}O = -2‰$ and only a single BO-type spherule plots between $\Delta^{17}O = -2‰$ and $\Delta^{17}O = 0‰$. Two spherules have data points plotting in both groups 2 and 4, suggesting a possible continuum between these groups.

When only carbonaceous/ordinary/enstatite chondrite and ^{16}O-poor parentages are considered, approximately 71% of our CSs are related to CCs, ~11% to ordinary
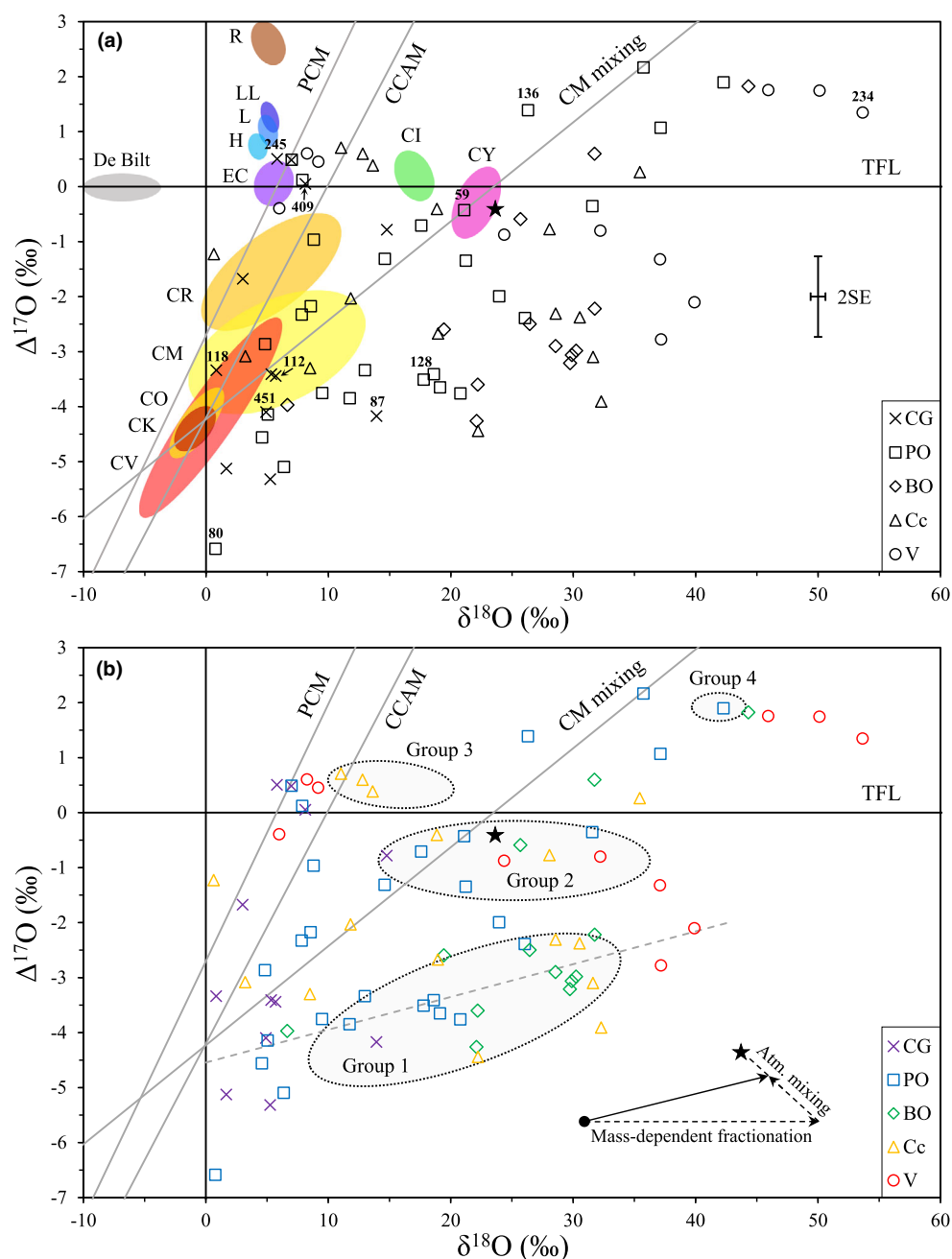
FIGURE 4. Plot of $\delta^{18}O$ versus $\Delta^{17}O$ of the 80 CSs from the Budel collection analyzed in this study. (a) Chondrite fields are adopted after Goderis et al. (2020) and Suavet et al. (2010) and based on literature data (Clayton et al., 1991; Clayton & Mayeda, 1999). The approximate range of CY chondrites is based on data from King et al. (2019) and Suttle, Greshake, et al. (2021). The composition of atmospheric oxygen is represented by an asterisk ($\delta^{18}O = 23.5‰$, $\Delta^{17}O = -0.42‰$; Thiemens et al., 1995). The PCM line (Ushikubo et al., 2012), CCAM line, and CM mixing line (Clayton & Mayeda, 1977, 1999) with slopes $\sim$0.987, $\sim$0.94, and $\sim$0.7, respectively, connect different chondrite parent bodies. The gray shaded area indicates the average annual oxygen isotopic composition of precipitation in De Bilt, the Netherlands (IAEA/WMO, 2022), which lies around the TFL (Clayton, 1993). The 2SE inset shows the average propagated analytical uncertainty for the data points. (b) The dotted line indicates the approximate trend along which spherules of group 1 evolve as a consequence of atmospheric mixing and mass-dependent fractionation with increasing $\delta^{18}O$ as CG < PO < BO < Cc < V. Gray ellipses show the major isotopic groups as defined by Suavet et al. (2010). The analyzed spherules define extended ranges of these groups: group (1) $\Delta^{17}O$ between $-3.5‰$ and $-5.5‰$ at $\delta^{18}O \approx 0‰$, increasing to between $-1‰$ and $-3‰$ at $\delta^{18}O \approx 40‰$; group, (2) $\Delta^{17}O$ between $-0.5‰$ and $-2‰$, and $\delta^{18}O$ between 0‰ and 35‰; group, (3) $\Delta^{17}O$ between 0.0‰ and 0.8‰, and $\delta^{18}O$ between 5‰ and 15‰; group, (4) $\Delta^{17}O$ between $\sim$0.2‰ and $\sim$2.2‰, and $\delta^{18}O$ between 25‰ and 55‰. Groups 2 and 4 form a continuum of ^{16}O-rich to ^{16}O-poor compositions dominated by the CM mixing line.

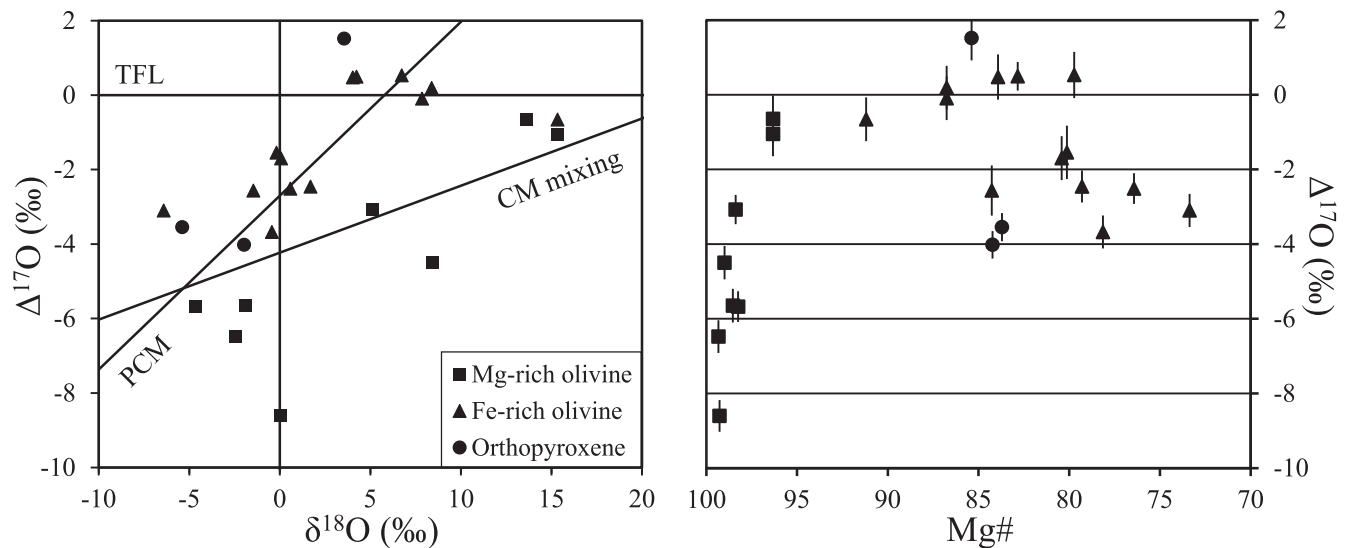FIGURE 5. Plot of $\delta^{18}O$ versus $\Delta^{17}O$ and Mg# versus $\Delta^{17}O$ of various relict minerals analyzed with no interference from adjacent mineral phases. Mg-rich olivine relicts generally plot near the CM mixing line (Clayton & Mayeda, 1999) and display a large range of $\Delta^{17}O$ values. Fe-rich olivine and Mg-rich orthopyroxene relicts mostly plot along the PCM line (Ushikubo et al., 2012) and are clustered with $\Delta^{17}O$ between $-2‰$ and $-4‰$ and between $0‰$ and $2‰$.

and/or enstatite chondrites, ~15% to ^{16}O-poor parentages, and ~3% is ambiguous (Table 3). Note that these values represent the parentage of the flux of CSs in the 100–500 μm size range and may be affected by selection bias. Ordinary/enstatite chondrites and HEDs cannot be discriminated with certainty considering the analytical uncertainties, but micrometeorites identified as originating from enstatite chondrites are in general exceedingly rare. Suttle et al. (2020) reported the first composite-type micrometeorite recognized as an enstatite chondritic micrometeorite but relied on an extensive study of the petrological characteristics of the particle, which is generally impossible in the case of melted CSs. Furthermore, no HED-like spherules have been confirmed. The low fractionation levels and vitreous texture of GMM84 (Table 1) are in accordance with a HED-like precursor, but additional analyses would be required to verify this (Cordier et al., 2012).

Relationships between Texture and Source

The abundances of different CS textures vary between oxygen isotopic groups. BO-type spherules occur predominantly, although not exclusively, in group 1 (Figure 4b). This indicates that the formation of a BO texture requires specific conditions and precursor characteristics. van Ginneken et al. (2017) suggested that a BO texture forms primarily from fine-grained CC matrices, which retain abundant submicron crystal nuclei during melting that favor the growth of barred olivine crystals. When few nuclei survive, a Cc texture is expected to form. Surprisingly, the various textural groups of the

Cc-type (microcrystalline, normal, and turtleback) all show equally large ranges for $\delta^{17}O$, $\delta^{18}O$, and $\Delta^{17}O$ and do not imply correlations to any specific precursor. Similarly, V-type spherules are most equally distributed among different isotopic groups (Table 3; Figure 4b), showing that they form from any precursor type once progressive heating destroys all nucleation sites (Rudraswami et al., 2020; van Ginneken et al., 2017).

Although represented in all major isotopic groups, the majority of our PO-type spherules, with diameters between 100 and 300 μm, show affinity to CCs (Table 3). In contrast, van Ginneken et al. (2017) found that PO-type spherules >500 μm in diameter commonly originate from OC precursors. As such, BO-type spherules appear to be the only exception to the general observation that the input of OC material becomes more dominant above 500 μm (Suavet et al., 2011; van Ginneken et al., 2017). This supports the hypothesis that BO-type spherules have one primary source material.

In accordance with these findings, micrometeorites of the Budel collection show that BO-type spherules occur as a unimodal size distribution with a major mode at ~170 μm. In contrast, both PO-type and Cc-type spherules display multimodal distributions with major modes at ~110 and ~130 μm, respectively, and several smaller shoulder peaks (fig. 4 in Jonker, van Elsas, et al., 2023). Separation biases are believed to be of minor significance (Jonker, van Elsas, et al., 2023). The occurrence of such shoulder peaks in the size distribution of CSs was interpreted by Suttle and Folco (2020) to indicate contributions from a variety of sources, each

with distinct particle size distributions. Considering the unimodal size distribution and the size-independent relation to CCs, it is therefore likely that the majority of BO-type spherules, or at least ~77%, originate from a single type of dust-producing parent body, possibly CO/CV/CK-like. JFCs that produce carbonaceous dust particles ~10–1000 μm in size (Nesvorný et al., 2010) could be a potential primary source for BO-type spherules, and thus group 1 spherules in general. Subsequently, if the remaining isotopic groups were to be sourced from a variety of carbonaceous and ordinary chondritic sources, either asteroids or comets, it could explain the large variation of isotopic compositions as well as the multimodal size distributions of most other textural groups (Jonker, van Elsas, et al., 2023).

PO textural subgroups show values different from normal PO-type spherules. We identified five μPO-type spherules of which four plot closely together with $\delta^{18}O$ between $17.8 \pm 0.6‰$ and $26.1 \pm 0.7‰$ and $\Delta^{17}O$ between $-3.8 \pm 0.9‰$ and $-2.0 \pm 1.0‰$ (e.g., GMM128; Figures 2c and 4). This is consistent with the hypothesis that μPO-type spherules have a fine-grained precursor similar to group 1 BO-type spherules and may thus be related to CV/CK-like chondrites (Goderis et al., 2020; van Ginneken et al., 2017). Additionally, we identified five PO-type spherules with cumulate textures (e.g., GMM136; Figures 2b and 4) as described by Genge, Suttle, et al. (2016), of which at least three have ^{16}O-poor compositions associated with group 4. This implies a potential link between the cumulate PO texture and the source of ^{16}O-poor particles.

Relationships between Mineralogy and Source

Figure 5 shows the oxygen isotopic composition of analyzed relict minerals of olivine and pyroxene and demonstrates the relation between $\Delta^{17}O$ and Mg#, expressed as mole% MgO/(FeO + MgO). Mg-rich olivine relicts with Mg# >95 plot mostly near the CM mixing line (Clayton & Mayeda, 1999). Fe-rich olivine and orthopyroxene relicts with Mg# <95 generally plot along the PCM line (Figure 5a). None of the Mg-rich olivine relicts plot above the TFL, indicating that these are generally related to CCs. Rudraswami, Suttle, et al. (2022) analyzed a large number of relict minerals in unmelted micrometeorites and PO-type spherules, including 68 Mg-rich olivines and three orthopyroxenes, and found that all anhydrous silicate relicts with $\Delta^{17}O > 0‰$ have Mg# <85. Accordingly, our results show the same pattern with relicts plotting on or above the TFL having Mg# ~80–85 (Figure 5).

The general trend observed in Figure 5b of increasing $\Delta^{17}O$ with decreasing Mg# is consistent with the trend found in minerals of various CCs and ferromagnesian Wild 2 comet particles (Connolly & Huss, 2010;

Nakashima et al., 2012; Rudraswami, Ushikubo, et al., 2011; Tenner et al., 2013; Ushikubo et al., 2012) and earlier studies on CSs (Engrand et al., 1999; Rudraswami et al., 2015). This trend is common in carbonaceous chondrules that formed from several reservoirs with distinct isotopic values in the outer solar system but absent in ordinary chondrules that formed in the inner solar system (Rudraswami, Suttle, et al., 2022). More specifically, relict minerals in micrometeorites with Mg# <90 are associated with type II chondrules, while those with Mg# >95 are associated with both type I and type II chondrules. Accordingly, spherules like GMM118 and GMM112 (Figure 1b,f) could be genetically related to type II chondrules, whereas GMM87 (Figure 1a) may be a typical example of type I. In addition, while relicts with Mg# >95 are generally consistent with CO and CM chondrules, the large range in $\Delta^{17}O$ for relicts with Mg# <90 is the most consistent with CR chondrules (Rudraswami, Suttle, et al., 2022). Relict minerals in CSs thus sample a variety of primarily CCs that formed from various isotopic reservoirs in the primordial solar nebula.

Several CSs exhibit atypical minerals. GMM451 (Figure 1c) is a CG-type spherule with minor Fe-rich olivine relicts and a large partially melted plagioclase relict, which are exceedingly rare in CSs (Taylor et al., 2011). Accessory phases include magnetite and Fe-Ni-S droplets. Oxygen isotope measurements show general homogeneity with average $\delta^{18}O = 4.9 \pm 1.0‰$ and $\Delta^{17}O = -4.1 \pm 1.2‰$ (Figure 4), excluding a genetic relation with ^{16}O-rich refractory inclusions, HED-like parentages, or other previously recognized plagioclase-rich basaltic achondritic parent bodies (Badjukov et al., 2010; Soens et al., 2022; Taylor et al., 2007). The mineralogy and isotopic signature indicate that this particle may have originated from plagioclase–olivine inclusions, which are isotopically less refractory than typical CAIs (Dai et al., 2021; Sheng et al., 1991).

GMM409 (Figure 1d), a CG-type spherule, contains a large Fe-rich olivine relict and a small (~10 μm) K-rich feldspar with ~13 wt% K_2O (Jonker, van Elsas, et al., 2023). The isotopic composition of the olivine relict plots near the TFL with average $\delta^{18}O = 8.1 \pm 0.6‰$ and $\Delta^{17}O = 0.1 \pm 0.8‰$ (Table 1; Figure 4). Considering the analytical uncertainty, GMM409 may thus originate from an ordinary, enstatite, carbonaceous (CR) chondritic, or achondritic parent body. Partial melting of the olivine relict and microtails at the surface indicate extensive heating and degassing (Suttle, Hasse, et al., 2021), while various concentric layers of different concentrations and sizes of magnetite crystals around the relict's periphery indicate significant oxygen exchange with the atmosphere (Taylor et al., 2011). Despite its comparatively low melting temperature relative to olivine, the K-rich feldspar shows limited signs of melting

(Figure 1d). K-rich feldspars have only been reported in iron meteorites (Bunch & Olsen, 1968; Wasserburg et al., 1968), which is not compatible with the mineralogy of the spherule. GMM409 could therefore have originated from an unknown source material. Alternatively, the feldspar crystal could have crystallized during atmospheric entry as volatile potassium interacted with the molten matrix of the particle. Although a terrestrial origin of GMM409 remains possible in terms of oxygen isotopic composition, the textural characteristics point to frictional heating in the atmosphere.

We found mineralogical and isotopic evidence for a genetic relation to meteoritic CAIs in GMM80, a rb-PO-type spherule with several Mg-rich olivine relicts (Figure 1g,h). A single olivine relict contains small ($<5\,\mu m$) globules which were found to be highly enriched in calcium (15.7 wt% CaO), aluminum (9.6 wt% Al_2O_3), and titanium (1.5 wt% TiO_2). All other EDS measurements on the particle indicated concentrations of these elements near or below detection limit. These globules indicate a possible genetic relation to refractory inclusions in CCs. Interestingly, a SIMS measurement partially overlapping a Mg-rich olivine relict showed strongly ^{16}O-enriched values of $\delta^{18}O = -27.7 \pm 0.4\%$ and $\delta^{17}O = -32.9 \pm 0.5\%$, which plots slightly to the right of the PCM line (Figure 3). Other relicts and recrystallized phases are characterized by compositions closer to the TFL, demonstrating significant isotopic heterogeneity. Such low oxygen isotope values have previously been reported in micrometeorites and are commonly associated with CAIs in CCs (Greshake et al., 1996; Rudraswami et al., 2015; Rudraswami, Suttle, et al., 2022; Soens et al., 2020; Taylor et al., 2011; Yada et al., 2005).

Origin of ^{16}O-Poor Micrometeorites

Group 4 micrometeorites with ^{16}O-poor compositions have not been correlated to any known chondrite parent body with certainty yet. The R chondrites or components of unequilibrated OCs (Choi et al., 1998; Franchi et al., 2001) were initially suggested by Suavet et al. (2010), but are unlikely based on the mineralogical and textural variability observed among group 4 particles (Goderis et al., 2020). Additionally, these sources would require extreme mass-dependent fractionation of oxygen, which is not indicated by the CS textures, the general absence of micrometeorites with compositions of $\Delta^{17}O > 1\%$ and $\delta^{18}O < 20\%$, and low chemical and iron isotope fractionation (Lampe et al., 2022; Suavet et al., 2011; Suttle et al., 2022). It is therefore commonly assumed that the precursor of group 4 particles is already ^{16}O depleted.

Suttle et al. (2022) found three low-heated relict-bearing micrometeorites with ^{16}O-poor compositions and suggested a genetic link to the CM mixing line

(Figure 4a). This line with a slope of 0.70 and $\delta^{17}O$ intercept at -4.23% connects the CM, CO, and recently identified CY chondrites, which reflect different extents of thermal metamorphism and ^{16}O depletion by aqueous alteration (Clayton & Mayeda, 1999; Suttle, Greshake, et al., 2021; Young, 2001). ^{16}O-poor micrometeorites frequently exceed the maximum $\Delta^{17}O$ values of $\sim 0.5\%$ reported for CY chondrites (Figure 4a) and may thus either extend the known range for CY chondrites or form a new endmember on this CM mixing line (Clayton & Mayeda, 1999; King et al., 2019; Suttle et al., 2022).

Consistent with earlier findings (e.g., Rudraswami et al., 2020), we find a variety of textures with ^{16}O-poor compositions associated with group 4 plotting above the TFL, including four PO-, a normal Cc-, two BO-, and three V-type spherules (Figure 4). The occurrence of ^{16}O-poor spherules with BO textures, previously linked to the fine-grained matrices of CCs (van Ginneken et al., 2017), further supports the suggested genetic relation of group 4 particles to the CM mixing line and CCs in general. Three of the four ^{16}O-poor PO-type spherules analyzed in this study display cumulate textures (Figure 2b), which were interpreted by Genge, Suttle, et al. (2016) as an indication of high eccentricity orbital parameters and high atmospheric entry speeds of up to $16\,km\,s^{-1}$. This apparent link between the cumulate texture and ^{16}O-poor compositions of some PO-type spherules provides clues to the characteristics of the parental source.

Assuming a genetic relation of at least some group 4 particles to aqueously altered CCs (i.e., the CM mixing line), with late overprinting of ^{16}O-rich compositions by heavy water, we may expect to find a continuum of ^{16}O-rich to ^{16}O-poor micrometeorites. We found evidence of the coexistence of ^{16}O-rich and ^{16}O-poor compositions in GMM87, a CG-type spherule (Figure 1a). A measurement on a forsterite relict yields $\delta^{18}O = 0.0 \pm 0.3\%$ and $\Delta^{17}O = -8.6 \pm 0.4\%$, plotting below typical bulk CCs, while the surrounding low-heated matrix yields ^{16}O-poor values of $\delta^{18}O = 27.8 \pm 0.3\%$ and $\Delta^{17}O = 0.3 \pm 0.3\%$, plotting near the CM mixing line and the group 4 field (Figure 4). This latter composition cannot be explained by mass-dependent fractionation and atmospheric mixing effects with the forsterite relict as starting composition, indicating that the matrix of this spherule must have been ^{16}O-poor before atmospheric entry. Fractures in the anhedral forsterite relicts indicate shock fragmentation caused by a large thermal gradient during atmospheric heating, which requires the presence of hydrated phyllosilicates that act as a heat sink through endothermic decomposition (Genge et al., 2017; Suttle et al., 2017). The presence of phyllosilicates and associated ^{16}O-depleted matrix compositions are typical of aqueously altered CCs (Zolensky et al., 2008). GMM87 could therefore be an example of extreme ^{16}O depletion through aqueous

alteration of the matrix of an originally ^{16}O-rich CC precursor.

A similar observation is made on GMM59 where an olivine relict gives $\delta^{18}O = 8.6 \pm 0.5‰$ and $\Delta^{17}O = -1.8 \pm 0.5‰$, while recrystallized phases show values as high as $\delta^{18}O = 31.8 \pm 0.3‰$ and $\Delta^{17}O = 0.6 \pm 0.4‰$. Again, atmospheric mixing and fractionation with the relict as the starting composition cannot explain the latter composition, so the matrix must have been ^{16}O-poor before atmospheric entry.

These heterogeneous spherules demonstrate that similar to meteorites, ^{16}O-poor matrices coexist with isotopically lighter anhydrous phases on a microscale and can be preserved in low-heated micrometeorites. At least some of the ^{16}O-poor spherules associated with group 4 may thus originate from isotopically heavy parts of aqueously altered CM/CO/CV/CK-like chondrites, rather than representing a previously unidentified chondrite group. This further supports the potential genetic link between ^{16}O-poor particles and the CM mixing line as proposed by Suttle et al. (2022). Yet, this does not fully explain why the most ^{16}O-depleted values are not encountered in larger meteorites. Finally, melting and subsequent homogenization of such heterogeneous micrometeoroids during atmospheric heating would result in isotopic compositions intermediate between groups 1, 2, and 4, demonstrating that averaged and bulk CSs isotopic compositions should be interpreted with care in terms of their relation to the major isotopic groups and potential sources.

Oxygen Isotopic Alteration

Terrestrial Alteration

Before attempting to quantify atmospheric alteration effects, it is important to assess the degree of terrestrial weathering and the associated isotopic alteration, which may obscure trends in atmospheric mixing and mass-dependent fractionation (e.g., Goderis et al., 2020; Suttle et al., 2020). The Dutch moderate maritime climate, which may cause weathering to occur within just a few years of exposure (Jonker, van Elsas, et al., 2023), is characterized by year-round precipitation with a long-term average oxygen isotopic composition of $\delta^{18}O = -7.4‰$ (De Bilt; Figure 4a; IAEA/WMO, 2022).

To determine whether terrestrial weathering could have altered the oxygen isotopic composition of the spherules, we have analyzed both weathered and pristine V-type spherules. The altered spherules are characterized by Mg-depleted weathering rinds that likely formed through contact with rainwater. Some spherules exhibit scalloped surfaces that formed as a result of etching underneath the weathering rinds and were exposed after

the rind was removed, either in the gutter or during sample processing (Jonker, van Elsas, et al., 2023).

Considering the analytical uncertainty of ~0.4‰– 0.5‰ and the small heterogeneities resulting from continuous isotopic fractionation during evaporation and quench crystallization, we do not observe any significant difference between values measured near the rim and the core of weathered spherules compared to pristine spherules. In addition, both pristine and altered V-type spherules generally show the highest $\delta^{18}O$ values of all textural types (Table 2; Figure 4) consistent with heating and evaporation models. Despite severe physical alteration of the surface of several of the analyzed V-type spherules, we thus find no evidence for any isotopic alteration. Since the remainder of our analyzed CSs population shows very little to no physical alteration, we assume that their isotopic values have not been significantly affected by terrestrial alteration.

Atmospheric Entry Effects

Within isotopic groups 1 and 2, Suavet et al. (2010) observed two trends of increasing $\Delta^{17}O$ with increasing $\delta^{18}O$. These trends relate the effects of kinetic mass-dependent fractionation, which shifts values to higher $\delta^{17}O$ and $\delta^{18}O$ parallel to the TFL, and mixing of intrinsic oxygen with atmospheric oxygen, which brings values closer to the isotopic composition of the upper atmosphere, changing $\delta^{17}O$, $\delta^{18}O$, and $\Delta^{17}O$ (Figure 4b; Clayton et al., 1986; Engrand et al., 2005; Rudraswami et al., 2020; Soens et al., 2022; Suavet et al., 2010; Taylor et al., 2005; Yada et al., 2005). Suavet et al. (2010) subsequently generally assigned isotopic groups 1 and 2 to CO/CV and CM/CR chondrites, respectively. In our analyzed population, we only observe such a correlation among the spherules plotting within the redefined group 1 field (dotted line in Figure 4b). There appears to be a general trend among group 1 spherules with $\Delta^{17}O$ around $-3.5‰$ to $-5.5‰$ at $\delta^{18}O \approx 0‰$ increasing to $\Delta^{17}O$ between $-1‰$ and $-3‰$ at $\delta^{18}O \approx 40‰$. The large scatter along this trend, likely resulting from the large variation in precursor compositions combined with the averaged spot data, complicates the determination of a strict correlation among these data points. Nonetheless, group 1 CSs show a general textural sequence with increasing $\delta^{18}O$ and $\Delta^{17}O$ as $CG < PO < BO \sim Cc < V$ (Table 2).

We find no evidence in our data set for the existence of a correlation among group 2 data points as indicated by Suavet et al. (2010). Rather the variation of isotopic compositions in these spherules seems to follow the CM mixing line, which partially overlaps with the CR chondrite compositions and continues into the group 4 field (Figure 4). Consequently, there is no consistent sequence of textural types with increasing $\delta^{18}O$ except for

TABLE 2. Average $\Delta^{17}O$ and $\delta^{18}O$ with 2SD of different spherule types belonging to group 1, and estimated extent of atmospheric mixing and evaporative oxygen loss uncorrected (f^a) and corrected (f^b) for atmospheric mixing (see main text).

Type	n	$\Delta^{17}O$ (‰)	2SD	Mixing (%)	2SD	$\delta^{18}O$ (‰)	2SD	f^a (%)	2SD	f^b (%)	2SD
CG	4	−4.5	1.8	0	[0–44]	4.3	3.5	17	[3–29]	17	[3–28]
PO	11	−3.8	1.4	18	[0–52]	13.9	14.2	45	[0–70]	34	[0–64]
BO	10	−3.1	1.3	34	[2–65]	24.7	15.2	65	[34–82]	51	[7–74]
Cc	6	−3.1	1.7	34	[0–76]	27.4	11.0	69	[50–80]	57	[31–73]
V	3	−2.1	1.5	60	[24–95]	38.1	3.2	80	[77–83]	64	[59–69]

Note: Isotopic values are given in permil (‰) relative to V-SMOW; mixing and oxygen loss are given in percent (%). Numbers between brackets are likely ranges for mixing and evaporation estimates based on 2SD uncertainties. Average $\delta^{18}O$ values are relative to the starting composition $\delta^{18}O_{pb}$ for which we adopt 0.0‰. Textural type: CG, coarse-grained (S-type); BO, barred olivine; Cc, cryptocrystalline; PO, porphyritic olivine; V, vitreous.

V-type spherules that generally plot farthest to the right of the CM mixing line.

Atmospheric Oxygen Exchange

Several attempts have been made to determine the extent of atmospheric oxygen admixture in S-type CSs using changes in $\delta^{18}O$ (Cordier et al., 2012; Soens et al., 2022). However, $\delta^{18}O$ is affected by both atmospheric mixing and mass-dependent fractionation, making it difficult to differentiate between these two processes without any additional analyses such as iron isotope ratios (Lampe et al., 2022; Soens et al., 2022). Based on such analyses, OC-derived spherules were shown to generally experience a ~8‰ shift in $\delta^{18}O$ as a result of atmospheric mixing (Lampe et al., 2022).

By focusing on $\Delta^{17}O$ instead, which is only influenced by atmospheric mixing and is largely independent of kinetic fractionation effects (Young et al., 2002), and assuming that no weathering has occurred, we have attempted to quantify the average extent of mixing for different CS types. We have only focused on the spherules of group 1 since most other isotopic groups cluster too close to atmospheric $\Delta^{17}O$ values to distinguish between atmospheric mixing and precursor heterogeneity. The calculation of the atmospheric admixture requires that the average starting composition of the CSs and the atmospheric composition are known. Modern atmospheric isotope values have been obtained directly by Thiemens et al. (1995) using a rocket-borne cryogenic whole air sampler for altitudes up to ~60 km and indirectly by Pack et al. (2017) using I-type micrometeorites, which incorporate oxygen through oxidation during atmospheric entry. These studies consistently indicate an atmospheric composition around $\delta^{18}O_{atm} \approx 23.5‰$, $\delta^{17}O_{atm} \approx 11.8‰$, and $\Delta^{17}O_{atm} \approx -0.42‰$. However, the actual $\delta^{18}O$ of atmospheric oxygen that is incorporated into CSs during mixing may

be ~8‰ lower than the true atmospheric value as a result of a kinetic isotope effect (Engrand et al., 2005), but this likely would not affect $\Delta^{17}O$. As bulk starting composition of the parent bodies, we assume that $\delta^{18}O_{pb} \approx 0.0$ and $\Delta^{17}O_{pb} \approx -4.5‰$, which plots within the CO/CV/CK fields and near the CCAM and CM mixing lines.

Assuming an open-system exchange of oxygen from CSs with the atmosphere, we can use the average $\Delta^{17}O$ of different CS textural groups ($\Delta^{17}O_{CS}$) to quantify the extent of mixing as:

$$\text{Atmospheric mixing}(\%) = \left[\left(\Delta^{17}O_{pb} - \Delta^{17}O_{CS}\right) / \left(\Delta^{17}O_{pb} - \Delta^{17}O_{atm}\right)\right] \times 100\%. \quad (1)$$

Average $\Delta^{17}O$ values with 2SD for CG-, PO-, BO-, Cc-, and V-type spherules belonging to group 1 are $-4.5 \pm 1.8‰$, $-3.8 \pm 1.4‰$, $-3.1 \pm 1.3‰$, $-3.1 \pm 1.7‰$, and $-2.1 \pm 1.5‰$, respectively. Using these values, we estimate atmospheric mixing components to be on average around 0% [0%–44%] for CG-type, 18% [0%–52%] for PO-type, 34% [2%–65%] for BO-type, 34% [0%–76%] for Cc-type, and 60% [24%–95%] for V-type spherules (Table 2). Numbers between brackets are based on 2SD uncertainties. These results provide a general indication of the amount of terrestrial oxygen within each CS. Changing the $\Delta^{17}O_{pb}$ by 0.1‰ only changes the mixing estimates by ~1%–2%. The results show that the average degree of atmospheric oxygen admixture increases as CG < PO < BO ~ Cc < V, which is consistent with the heating sequence proposed by Taylor et al. (2000). This demonstrates that, at least for group 1 spherules, the extent of atmospheric mixing is linked to the quench texture and subsequently increases as a function of peak temperature and duration of heating during atmospheric entry.

Evaporation and Kinetic Mass-Dependent Fractionation

The extent of evaporation and associated mass loss responsible for mass-dependent fractionation has frequently been discussed. Love and Brownlee (1991) suggested total mass losses of 70%–90% for CSs based on atmospheric entry models. By applying the Rayleigh equation to isotopes of Fe, Mg, and Si, Alexander et al. (2002) found total evaporative mass losses of up to 50% for the most heated CAT spherules, while Engrand et al. (2005) derived oxygen losses of 50%–70% for BO-type spherules of groups 1 and 2, or 10%–20% for BO- and PO-type spherules originating from CI chondrites. Using a comparative study of major and trace elements, Cordier et al. (2011) concluded total evaporative losses of 50%–70% for CAT-like spherules and 40%–50% for normal V-type spherules, while Goderis et al. (2020) reported ∼50% mass loss for CAT-like and >75% for high Ca-Al spherules. Chemical fractionation may, however, be an inadequate proxy for evaporation due to biases resulting from precursor heterogeneity, metal bead segregation and ejection, or terrestrial alteration (Lampe et al., 2022).

For our calculations, we have based our approach on the methods of Cordier et al. (2012), who calculated the oxygen loss by evaporation (f) using the Rayleigh fractionation equation:

$$f(\%) = \left(1 - \left(\delta^{18}O_{CS}/1000 + 1\right)^{(\alpha/(1-\alpha))}\right) \times 100\%. \quad (2)$$

$\delta^{18}O_{CS}$ indicates the degree of mass-dependent fractionation relative to the bulk starting composition, for which we assume $\delta^{18}O_{pb} \approx 0.0‰$ (CO/CV/CK fields) for group 1 CSs. We use a kinetic fractionation factor $\alpha = 1.0237$ for $^{18}O/^{16}O$, as experimentally determined for high-temperature evaporation of materials with a solar composition (Wang et al., 2001).

Average $\delta^{18}O$ values with 2SD for CG-, PO-, BO-, Cc-, and V-type spherules belonging to group 1 are $4.3 \pm 3.5‰$, $13.9 \pm 14.2‰$, $24.7 \pm 15.2‰$, $27.4 \pm 11.0‰$, and $38.1 \pm 3.2‰$, respectively. Using Equation (2), the oxygen loss through evaporation would thus be on average 17% [3%–29%] for CG-type, 45% [0%–70%] for PO-type, 65% [34%–82%] for BO-type, 69% [50%–80%] for Cc-type, and 80% [77%–83%] for V-type spherules. Numbers between brackets indicate the likely ranges based on 2SD uncertainties. Changing the starting composition ($\delta^{18}O_{pb}$) by 1‰ changes the estimates by at most ∼3%, decreasing as total fractionation increases. The uncertainty of the precursor composition therefore does not significantly alter the estimated oxygen evaporation. The propagated 2SE analytical uncertainties of ∼0.6‰ will have an equally limited effect on our estimates. Note that the results for CG-type spherules are questionable since the Rayleigh equation assumes a homogeneous material, which is usually not the case due to the presence of abundant relicts.

The admixture of atmospheric oxygen affects $\delta^{18}O$ of a micrometeoroid, which should also be considered. According to Clayton et al. (1986), atmospheric mixing results in an increase in $\delta^{18}O$ of ∼8‰ in the fusion crusts of meteorites, which has previously been used to correct for mixing effects (Cordier et al., 2012; Lampe et al., 2022; Soens et al., 2022). However, this correction was shown by Lampe et al. (2022) to be at least in part unsuitable for CSs, partly because various types of CSs experience different degrees of mixing.

The shift in $\delta^{18}O$ by atmospheric mixing depends on the composition of the CS relative to the atmospheric composition and thus depends on its concurrence with mass-dependent fractionation. The increase in $\delta^{18}O$ through mixing will be most pronounced when mixing occurs prior to mass-dependent fractionation. Thus, to obtain lower bound estimates of oxygen evaporation, we use our mixing estimates to determine the maximum shift in $\delta^{18}O$ possible, which we subsequently subtract from $\delta^{18}O_{CS}$ in Equation (2). This correction provides lower bound estimates of average oxygen evaporation of 17% for CG-type, 34% for PO-type, 51% for BO-type, 57% for Cc-type, and 64% for V-type spherules (Table 2). However, since mixing most likely concurs with mass-dependent fractionation, the actual effect of atmospheric mixing is presumably less. In addition, as demonstrated by Engrand et al. (2005), the actual $\delta^{18}O$ of atmospheric oxygen incorporated into CSs may be ∼8‰ lower than the true $\delta^{18}O_{atm}$ as a result of a kinetic isotope effect, in which case $\delta^{18}O$ shift from mixing would be even more reduced. To conclude, the true values of oxygen evaporation are expected to lie in between our corrected and uncorrected estimates.

Our results for BO-type spherules with on average 51%–65% oxygen evaporation are in close agreement with the results of Engrand et al. (2005), who derived oxygen losses of 50%–70% for BO-type spherules of groups 1 and 2. The results are also consistent with Suavet et al. (2010), who found fractionation levels of up to ∼50‰ for group 1 BO-type spherules associated with up to ∼60% atmospheric mixing. The evaporative oxygen losses shown here are linked to, but not indicative of, total mass loss since the fractionation behavior of different elements varies (Alexander et al., 2002; Engrand et al., 2005; Lampe et al., 2022; Rudraswami, Pandey, et al., 2022; Wang et al., 2001).

The trend in group 1 of increasing oxygen evaporation with CS texture as CG < PO < BO < Cc < V is consistent with the general notion that CSs textures reflect the peak temperature reached during atmospheric

deceleration (Engrand et al., 2005; Rudraswami et al., 2020; Taylor et al., 2000, 2005).

For groups 2, 3, and 4, the effects of mixing are unknown and the starting compositions are less well-defined. Hence, evaporative loss estimates carry large uncertainties. Nonetheless, for comparison, we determined the evaporative loss of V-type spherules of the remaining groups without mixing correction. For this, the respective $\delta^{18}O$ starting compositions of V-type spherules from groups 2, 3, and 4 are assumed to be around 0.0‰–20.0‰ (CR or CM mixing line), 5.0‰ (LL/L/H), and 32.5‰ (CM mixing line), respectively. Average evaporative losses using these starting compositions are ~30%–70%, ~15%, and ~53%, respectively. Losses for groups 2 and 3 are upper bounds, while the loss determined for group 4 is a lower bound since mixing will only lower $\delta^{18}O$. Thus, while evaporative losses within groups 2 and 4 are comparable with group 1, evaporative losses within group 3 are much smaller. Our ~15% oxygen evaporation estimate for group 3 V-type spherules is consistent with the 10%–40% reported by Lampe et al. (2022) for OC-derived V-type spherules of group 3, but lower than the 30%–50% reported by Cordier et al. (2012) and 30%–80% reported by Soens et al. (2022) for HED-like CSs. The comparatively limited evaporation of group 3 CSs may be related to pronounced petrological and chemical differences between carbonaceous, ordinary, and enstatite chondrites and HEDs such as the volatility, with high volatilities enhancing evaporation (Rudraswami et al., 2020). This could explain why cosmic dust particles sourced from hydrated CC precursors usually experience stronger fractionation during atmospheric entry than particles sourced from mostly anhydrous precursors.

A comparative study by Engrand et al. (2005) concluded that I-type spherules experience more oxygen evaporation than S-type spherules as a result of (1) reduced heating of S-type CSs with highly volatile contents; (2) higher evaporation temperatures of anhydrous/refractory silicates relative to iron metals and oxides; (3) faster deceleration with shorter heating pulse of comparatively low-density S-type CSs. Engrand et al. (2005) reported evaporative losses of ~55%–77% in I-type spherules, similar to earlier results of Herzog et al. (1999) of ~62%–73%. However, our results of evaporative losses of group 1 BO-, Cc-, and V-type spherules (on average 65%, 69%, and 80%, respectively), as well as V-type spherules of groups 2 and 4 (~30%–70% and ~53%, respectively) are comparable to the results on I-type spherules. Note that Engrand et al. (2005) primarily targeted S-type spherules with PO textures which consistently experience comparatively lower fractionation levels. The level of oxygen evaporation of I-type spherules therefore corresponds to the most heated S-type spherules.

Contemporary Micrometeorite Flux

The CSs of the Budel collection used for this study were accreted to the Earth between October 31, 2018 and June 16, 2021, and thus provide a direct sample of the present-day flux of micrometeorites. Table 3 reports the parentage statistics of this work compared to compiled literature data (references in caption). Taking into account that assigning CSs to specific precursors comes with significant uncertainties, our results are broadly compatible with earlier studies on older collections, in particular the similarly extensive study by Rudraswami et al. (2020). This demonstrates that the cosmic dust flux to the Earth does not change significantly over thousand- to million-year time scales.

The contribution of CR clan chondrites as the main source of group 2 particles was discussed by Goderis et al. (2020), who reportedly found only ~4% of their analyzed population to belong to group 2. A comparison to the ~21% (Suavet et al., 2010) and ~17% (van Ginneken et al., 2017) of comparable collections with large >500 μm CSs indicated a potential change in the micrometeorite flux. However, with the much larger isotopic range of group 2 defined by our measurements on CSs <500 μm in size, about 14%–21% of CSs analyzed by Goderis et al. (2020) could be assigned to group 2. These results are compatible with the ~17.5% of group 2 spherules reported herein. In addition, we have shown that many group 2 spherules may be genetically related to both CR chondrites as well as the CM mixing line and that the boundaries of group 2 are somewhat ambiguous in relation to groups 1 and 4. Considering these uncertainties, the relative abundances of group 2 spherules in various collections do not suggest significant fluctuations in the contribution of CR clan chondrites to the micrometeorite flux over the last several million years.

The existence of ^{16}O-poor particles in micrometeorite collections has long been acknowledged by multiple independent studies (Goderis et al., 2020; Lampe et al., 2022; Rudraswami, Prasad, Dey, et al., 2016; Rudraswami et al., 2020; Suavet et al., 2010, 2011; Suttle et al., 2020, 2022; van Ginneken et al., 2017, 2022; van Maldeghem et al., 2023; Yada et al., 2005). The micrometeorites analyzed in these studies originate from various collections that record a large variation in terms of size fractions, geographic locations, and terrestrial ages. Cordier and Folco (2014) showed that ^{16}O-poor particles occur in most size fractions, but are generally most abundant in the smaller size fractions <250 μm. The oldest collection to record ^{16}O-poor compositions consists of micrometeorites recovered from the Atacama Desert, which has collection times of >5 Myr (Hutzler et al., 2016; van Ginneken et al., 2017). Antarctic collections of intermediate age include the Widerøefjellet

TABLE 3. Statistics of parent body affinity for various size fractions and different spherule textures.

Affinity	OC	CC	^{16}O-poor	Ambiguous	HED	Total
# of spherules (this study)	9	57	12	2	0	80
% all sizes	11	71	15	3	0	
% 100–250	11	73	14	2	0	56
% 250–500	13	65	17	4	0	23
% 500–1000	0	100	0	0	0	1
% CG	17	75	0	8	0	12
% PO	7	71	21	0	0	28
% BO	0	85	15	0	0	13
% Cc	19	75	6	0	0	16
% V	18	45	27	9	0	11
# of spherules (literature)	50	128	21	26	6	231
% all sizes	22	55	9	11	3	
% <100	7	66	17	10	0	29
% 100–250	12	59	11	18	0	39
% 250–500	20	68	6	6	0	66
% 500–1000	30	46	7	10	7	86
% >1000	36	18	18	27	0	11

Note: Totals are expressed as number of spherules. Textural type: BO, barred olivine; Cc, cryptocrystalline; CG, coarse-grained (S-type); PO, porphyritic olivine; V, vitreous. Parent affinity: CC, carbonaceous chondrite; HED, howardite/eucrite/diogenite; OC, ordinary chondrite. Literature data are derived from Cordier and Folco (2014) and references therein, and Goderis et al. (2020), Lampe et al. (2022), Suttle et al. (2020), and van Ginneken et al. (2017).

collection of ~1–3 Ma (Goderis et al., 2020), the TAM collections of ~1 Ma (Rochette et al., 2008), and micrometeorites recovered from the Yamato Mountains, dating from the last glacial maximum (Machida et al., 1996; Yada & Kojima, 2000). Rudraswami et al. (2020) performed an extensive oxygen isotope study on micrometeorites from several relatively young collections and found ^{16}O-poor signatures in each. These collections include CSs recovered from the Indian Ocean with collection times of up to ~50 kyr (Prasad et al., 2013), Antarctic blue ice (Rudraswami et al., 2018), and the Antarctic South Pole water well, which has the youngest terrestrial age of 430 ± 50 years (Taylor et al., 1998).

With a relative abundance of ~13%–15%, we here show for the first time that ^{16}O-poor particles still occur in the contemporary flux of cosmic dust accreted to the Earth between October 31, 2018 and June 16, 2021. While their exact origin remains yet unresolved, the occurrence of ^{16}O-poor spherules in our analyzed population illustrates that the reservoir from which they originate remains an important contributor to the Zodiacal cloud and that the accretion of ^{16}O-poor material was not an isolated event in Earth's history, but continues to this day.

CONCLUSIONS

We present the results of an extensive oxygen isotopic study on rooftop micrometeorites of the Budel collection through 213 in situ analyses on both relict and recrystallized phases using SIMS on 80 S-type CSs representing all textural groups except CAT. In situ measurements are characterized by a large range in isotopic compositions from highly ^{16}O-rich (δ^{18}O = −27.7‰) to ^{16}O-poor (δ^{18}O = 54.7‰). Our results extend the ranges of the isotopic groups previously defined by Suavet et al. (2010). Roughly 71% of our analyzed population is associated with CC precursors, 11% with ordinary or enstatite chondrites, and 15% with a ^{16}O-poor origin. ~3% of the spherules are ambiguous and cannot be correlated to a specific precursor.

The unimodal size distribution of BO-type spherules, combined with their primarily CO/CV/CK-like isotopic signature associated with group 1, has been used to argue that this type of spherule is likely predominantly sourced from a single type of parent body, possibly JFCs. However, two BO-type spherules exhibit ^{16}O-poor compositions, suggesting a genetic link between group 4 particles and CCs. ^{16}O-rich and ^{16}O-poor compositions are also found to coexist within relict-bearing CSs, demonstrating that at least some group 4 particles may originate from the aqueously altered matrices of initially ^{16}O-rich chondritic bodies.

PO-type spherules with microporphyritic textures, previously interpreted to form from a similar type of precursor material as BO-type spherules, show isotopic values close to those of BO-type spherules. PO-type spherules with cumulate textures frequently record ^{16}O-poor compositions, possibly indicating high eccentricity orbits and high entry velocities for some of the ^{16}O-poor

particles. Cc- and V-type spherules show the widest range in isotopic compositions and form from any type of precursor.

Within V-type spherules selected for their pronounced characteristics of terrestrial weathering, we found no evidence of significant isotopic alteration. The effects of terrestrial alteration in rooftop micrometeorites are therefore assumed to be generally negligible. However, the oxygen isotopic compositions of CSs record progressive stages of kinetic mass-dependent fractionation and atmospheric mixing which is reflected in their quench textures. For group 1 CSs, the extent of mixing increases up to ~60% for the most heated V-type spherules. The degree of kinetic fractionation of group 1 CSs increases as $CG < PO < BO < Cc < V$, with respective estimated evaporative oxygen losses of 17%, 45%, 65%, 69%, and 80%. CSs of groups 2 and 4 likely experienced evaporative losses similar to the CSs of group 1. CSs derived from OCs are shown to have experienced much lower levels of mass-dependent fractionation than CSs derived from CCs.

The extremely young and well-constrained terrestrial age of the Budel collection, which accreted to Earth between October 31, 2018 and June 16, 2021, allows us to assess the oxygen isotopic data in relation to thousand- to million-year-old collections. Our results indicate no major changes in the cosmic dust flux compared to the long-term average and demonstrate that ^{16}O-poor material is still accreting to the Earth up to the present day. The Budel rooftop micrometeorite collection complements existing collections of different origins and offers the opportunity to study the most recent cosmic dust accreted to the Earth.

Data Availability Statement—The data that support the findings of this study are available in the supplementary material of this article. Data related to the Budel collection are available in DataverseNL at 10.34894/EKEXD6 (Jonker, Schipper, et al., 2023).

Editorial Handling—Dr. Donald E. Brownlee

REFERENCES

Alexander, C. M. O'D., Taylor, S., Delaney, J. S., Ma, P., and Herzog, G. F. 2002. Mass-Dependent Fractionation of Mg, Si, and Fe Isotopes in Five Stony Cosmic Spherules. *Geochimica et Cosmochimica Acta* 66: 173–183. https://doi.org/10.1016/S0016-7037(01)00764-5.

Badjukov, D. D., Brandstätter, F., Raitala, J., and Kurat, G. 2010. Basaltic Micrometeorites from the Novaya Zemlya Glacier. *Meteoritics & Planetary Science* 45: 1502–12. https://doi.org/10.1111/j.1945-5100.2010.01125.x.

Bland, P. A., Smith, T. B., Jull, A. J. T., Berry, F. J., Bevan, A. W. R., Cloudt, S., and Pillinger, C. T. 1996. The Flux of Meteorites to the Earth over the Last 50,000 Years. *Monthly Notices of the Royal Astronomical Society* 283: 551–565. https://doi.org/10.1093/mnras/283.2.551.

Brase, L. E., Harvey, R., Folco, L., Suttle, M. D., McIntosh, E. C., Day, J. M. D., and Corrigan, C. M. 2021. Microtektites and Glassy Cosmic Spherules from New Sites in the Transantarctic Mountains, Antarctica. *Meteoritics & Planetary Science* 56: 829–843. https://doi.org/10.1111/maps.13634.

Brownlee, D. E., Bates, B., and Schramm, L. 1997. The Elemental Composition of Stony Cosmic Spherules. *Meteoritics & Planetary Science* 32: 157–175. https://doi.org/10.1111/j.1945-5100.1997.tb01257.x.

Bunch, T. E., and Olsen, E. 1968. Potassium Feldspar in Weekeroo Station, Kodaikanal, and Colomera Iron Meteorites. *Science* 160: 1223–25. https://doi.org/10.1126/science.160.3833.1223.

Choi, B. G., McKeegan, K. D., Krot, A. N., and Wasson, J. T. 1998. Extreme Oxygen-Isotope Compositions in Magnetite from Unequilibrated Ordinary Chondrites. *Nature* 392: 577–79. https://doi.org/10.1038/33356.

Clayton, R. N. 1993. Oxygen Isotopes in Meteorites. *Annual Review of Earth and Planetary Sciences* 21: 115–149. https://doi.org/10.1146/annurev.ea.21.050193.000555.

Clayton, R. N., and Mayeda, T. K. 1977. Correlated Oxygen and Magnesium Isotope Anomalies in Allende Inclusions, I: Oxygen. *Geophysical Research Letters* 4: 295–98. https://doi.org/10.1029/GL004i007p00295.

Clayton, R. N., and Mayeda, T. K. 1999. Oxygen Isotope Studies of Carbonaceous Chondrites. *Geochimica et Cosmochimica Acta* 63: 2089–2104. https://doi.org/10.1016/S0016-7037(99)00090-3.

Clayton, R. N., Mayeda, T. K., and Brownlee, D. E. 1986. Oxygen Isotopes in Deep-Sea Spherules. *Earth and Planetary Science Letters* 79: 235–240. https://doi.org/10.1016/0012-821X(86)90181-0.

Clayton, R. N., Mayeda, T. K., Goswami, J. N., and Olsen, E. J. 1991. Oxygen Isotope Studies of Ordinary Chondrites. *Geochimica et Cosmochimica Acta* 55: 2317–37. https://doi.org/10.1016/0016-7037(91)90107-G.

Connolly, H. C., and Huss, G. R. 2010. Compositional Evolution of the Protoplanetary Disk: Oxygen Isotopes of Type-II Chondrules from CR2 Chondrites. *Geochimica et Cosmochimica Acta* 74: 2473–83. https://doi.org/10.1016/j.gca.2010.01.005.

Cordier, C., and Folco, L. 2014. Oxygen Isotopes in Cosmic Spherules and the Composition of the Near Earth Interplanetary Dust Complex. *Geochimica et Cosmochimica Acta* 146: 18–26. https://doi.org/10.1016/j.gca.2014.09.038.

Cordier, C., Folco, L., Suavet, C., Sonzogni, C., and Rochette, P. 2011. Major, Trace Element and Oxygen Isotope Study of Glass Cosmic Spherules of Chondritic Composition: The Record of their Source Material and Atmospheric Entry Heating. *Geochimica et Cosmochimica Acta* 75: 5203–18. https://doi.org/10.1016/j.gca.2011.06.014.

Cordier, C., Suavet, C., Folco, L., Rochette, P., and Sonzogni, C. 2012. HED-Like Cosmic Spherules from the Transantarctic Mountains, Antarctica: Major and Trace Element Abundances and Oxygen Isotopic Compositions. *Geochimica et Cosmochimica Acta* 77: 515–529. https://doi.org/10.1016/j.gca.2011.10.021.

Criss, R. E., and Farquhar, J. 2008. Abundance, Notation, and Fractionation of Light Stable Isotopes. *Reviews in Mineralogy and Geochemistry* 68: 15–30. https://doi.org/10.2138/rmg.2008.68.3.

Dai, D., Bao, H., Liu, S., and Yin, F. 2021. Oxygen Isotopic Compositions in a Plagioclase-Olivine Inclusion from Ningqiang Similar to those in Al-Rich Chondrules. *Acta Geologica Sinica* 95: 1583–90. https://doi.org/10.1111/1755-6724.14682.

Duprat, J., Engrand, C., Maurette, M., Kurat, G., Gounelle, M., and Hammer, C. 2007. Micrometeorites from Central Antarctic Snow: The CONCORDIA Collection. *Advances in Space Research* 39: 605–611. https://doi.org/10.1016/j.asr.2006.05.029.

Engrand, C., McKeegan, K. D., and Leshin, L. A. 1999. Oxygen Isotopic Compositions of Individual Minerals in Antarctic Micrometeorites: Further Links to Carbonaceous Chondrites. *Geochimica et Cosmochimica Acta* 63: 2623–36. https://doi.org/10.1016/S0016-7037(99)00160-X.

Engrand, C., McKeegan, K. D., Leshin, L. A., Herzog, G. F., Schnabel, C., Nyquist, L. E., and Brownlee, D. E. 2005. Isotopic Compositions of Oxygen, Iron, Chromium, and Nickel in Cosmic Spherules: Toward a Better Comprehension of Atmospheric Entry Heating Effects. *Geochimica et Cosmochimica Acta* 69: 5365–85. https://doi.org/10.1029/2020JE006414.

Faul, H., and Davis, G. L. 1959. Mineral Separation with Asymmetric Vibrators. *American Mineralogist* 44: 1076–82.

Franchi, I. A. 2008. Oxygen Isotopes in Asteroidal Materials. *Reviews in Mineralogy and Geochemistry* 68: 345–397. https://doi.org/10.2138/rmg.2008.68.13.

Franchi, I. A., Baker, L., Bridges, J. C., Wright, I. P., and Pillinger, C. T. 2001. Oxygen Isotopes and the Early Solar System. *Philosophical Transactions of the Royal Society of London Series A: Mathematical, Physical and Engineering Sciences* 359: 2019–35. https://doi.org/10.1098/rsta.2001.0894.

Genge, M. J., Engrand, C., Gounelle, M., and Taylor, S. 2008. The Classification of Micrometeorites. *Meteoritics & Planetary Science* 43: 497–515. https://doi.org/10.1111/j.1945-5100.2008.tb00668.x.

Genge, M. J., Larsen, J., van Ginneken, M., and Suttle, M. D. 2016. An Urban Collection of Modern-Day Large Micrometeorites: Evidence for Variations in the Extraterrestrial Dust Flux through the Quaternary. *Geology* 45: 119–122. https://doi.org/10.1130/G38352.1.

Genge, M. J., Suttle, M. D., and van Ginneken, M. 2016. Olivine Settling in Cosmic Spherules during Atmospheric Deceleration: An Indicator of the Orbital Eccentricity of Interplanetary Dust. *Geophysical Research Letters* 43: 10646–53. https://doi.org/10.1002/2016GL070874.

Genge, M. J., Suttle, M. D., and van Ginneken, M. 2017. Thermal Shock Fragmentation of Mg Silicates within Scoriaceous Micrometeorites Reveal Hydrated Asteroidal Sources. *Geology* 45: 891–94. https://doi.org/10.1130/G39426.1.

Genge, M. J., van Ginneken, M., and Suttle, M. D. 2020. Micrometeorites: Insights into the Flux, Sources and Atmospheric Entry of Extraterrestrial Dust at Earth. *Planetary and Space Science* 187: 104900. https://doi.org/10.1016/j.pss.2020.104900.

Genge, M. J., van Ginneken, M., Suttle, M. D., and Harvey, R. P. 2018. Accumulation Mechanisms of Micrometeorites in an Ancient Supraglacial Moraine at Larkman Nunatak, Antarctica. *Meteoritics & Planetary Science* 53: 2051–66. https://doi.org/10.1111/maps.13107.

Goderis, S., Soens, B., Huber, M. S., McKibbin, S., van Ginneken, M., van Maldeghem, F., Debaille, V., et al. 2020. Cosmic Spherules from Widerøefjellet, Sør Rondane Mountains (East Antarctica). *Geochimica et Cosmochimica Acta* 270: 112–143. https://doi.org/10.1016/j.gca.2019.11.016.

Gounelle, M., Engrand, C., Maurette, M., Kurat, G., McKeegan, K. D., and Brandstätter, F. 2005. Small Antarctic Micrometeorites: A Mineralogical and In Situ Oxygen Isotope Study. *Meteoritics & Planetary Science* 40: 917–932. https://doi.org/10.1111/j.1945-5100.2005.tb00163.x.

Greshake, A., Bischoff, A., and Hoppe, P. 1996. Mineralogy, Chemistry, and Oxygen Isotopes of Refractory Inclusions from Stratospheric Interplanetary Dust Particles and Micrometeorites. *Meteoritics & Planetary Science* 31: 739–748. https://doi.org/10.1111/j.1945-5100.1996.tb02109.x.

Herzog, G. F., Xue, S., Hall, G. S., Nyquist, L. E., Shih, C. Y., Wiesmann, H., and Brownlee, D. E. 1999. Isotopic and Elemental Composition of Iron, Nickel, and Chromium in Type I Deep-Sea Spherules: Implications for Origin and Composition of the Parent Micrometeoroids. *Geochimica et Cosmochimica Acta* 63: 1443–57. https://doi.org/10.1016/S0016-7037(99)00011-3.

Hutzler, A., Gattacceca, J., Rochette, P., Braucher, R., Carro, B., Christensen, E. J., Cournede, C., et al. 2016. Description of a Very Dense Meteorite Collection Area in Western Atacama: Insight into the Long-Term Composition of the Meteorite Flux to Earth. *Meteoritics & Planetary Science* 51: 468–482. https://doi.org/10.1111/maps.12607.

IAEA/WMO. 2022. Global Network of Isotopes in Precipitation: The GNIP Database https://nucleus.iaea.org/wiser.

IJlst, L. 1973. A Laboratory Overflow-Centrifuge for Heavy Liquid Mineral Separation. *American Mineralogist* 58: 1088–93.

Imae, N., Taylor, S., and Iwata, N. 2013. Micrometeorite Precursors: Clues from the Mineralogy and Petrology of their Relict Minerals. *Geochimica et Cosmochimica Acta* 100: 116–157. https://doi.org/10.1016/j.gca.2012.09.052.

Jonker, G., Schipper, T., Tuithof, J., van der Lubbe, H. J. L., van Elsas, R., Haak, M., and van Westrenen, W. 2023. Rooftop Micrometeorites from the Budel Collection, the Netherlands *DataverseNL.* https://doi.org/10.34894/EKEXD6.

Jonker, G., van Elsas, R., van der Lubbe, H. J. L., and van Westrenen, W. 2023. Improved Collection of Rooftop Micrometeorites through Optimized Extraction Methods: The Budel Collection. *Meteoritics & Planetary Science* 58: 463–479. https://doi.org/10.1111/maps.13966.

King, A. J., Bates, H. C., Krietsch, D., Busemann, H., Clay, P. L., Schofield, P. F., and Russell, S. S. 2019. The Yamato-Type (CY) Carbonaceous Chondrite Group: Analogues for the Surface of Asteroid Ryugu? *Geochemistry* 79: 125531. https://doi.org/10.1016/j.chemer.2019.08.003.

Lampe, S., Soens, B., Chernonozhkin, S. M., de Vega, C. G., van Ginneken, M., van Maldeghem, F., Vanhaecke, F., et al. 2022. Decoupling of Chemical and Isotope Fractionation Processes during Atmospheric Heating of Micrometeorites. *Geochimica et Cosmochimica Acta* 324: 221–239. https://doi.org/10.1016/j.gca.2022.02.008.

Love, S. G., and Brownlee, D. E. 1991. Heating and Thermal Transformation of Micrometeoroids Entering the Earth's Atmosphere. *Icarus* 89: 26–43. https://doi.org/10.1016/0019-1035(91)90085-8.

Love, S. G., and Brownlee, D. E. 1993. A Direct Measurement of the Terrestrial Mass Accretion Rate of Cosmic Dust. *Science* 262: 550–53. https://doi.org/10.1126/science.262.5133.550.

Machida, T., Nakazawa, T., Narita, H., Fujii, Y., Aoki, S., and Watanabe, O. 1996. Variations of the CO_2, CH_4 and N_2O Concentrations and $\delta^{13}C$ of CO_2 in the Glacial Period Deduced from an Antarctic Ice Core, South Yamato. *Proceedings of the NIPR Symposium on Polar Meteorology and Glaciology* 10: 55–65.

Matrajt, G., Guan, Y., Leshin, L., Taylor, S., Genge, M. J., Joswiak, D., and Brownlee, D. E. 2006. Oxygen Isotope Measurements of Individual Unmelted Antarctic Micrometeorites. *Geochimica et Cosmochimica Acta* 70: 4007–18. https://doi.org/10.1016/j.gca.2006.05.010.

Maurette, M., Olinger, C., Michel-Levy, M. C., Kurat, G., Pourchet, M., Brandstätter, F., and Bourot-Denise, M. 1991. A Collection of Diverse Micrometeorites Recovered from 100 tonnes of Antarctic Blue Ice. *Nature* 351: 44–47. https://doi.org/10.1038/351044a0.

Nakashima, D., Ushikubo, T., Joswiak, D. J., Brownlee, D. E., Matrajt, G., Weisberg, M. K., Zolensky, M. E., and Kita, N. T. 2012. Oxygen Isotopes in Crystalline Silicates of Comet Wild 2: A Comparison of Oxygen Isotope Systematics between Wild 2 Particles and Chondritic Materials. *Earth and Planetary Science Letters* 357-358: 355–365. https://doi.org/10.1016/j.epsl.2012.09.041.

Nesvorný, D., Jenniskens, P., Levison, H. F., Bottke, W. F., Vokrouhlický, D., and Gounelle, M. 2010. Cometary Origin of the Zodiacal Cloud and Carbonaceous Micrometeorites. Implications for Hot Debris Disk. *The Astrophysical Journal* 713: 816. https://doi.org/10.1088/0004-637X/713/2/816.

Pack, A., Höweling, A., Hezel, D. C., Stefanak, M. T., Beck, A. K., Peters, S. T. M., Sengupta, S., Herwartz, D., and Folco, L. 2017. Tracing the Oxygen Isotope Composition of the Upper Earth's Atmosphere Using Cosmic Spherules. *Nature Communications* 8: 15702. https://doi.org/10.1038/ncomms15702.

Prasad, M. S., Rudraswami, N. G., and Panda, D. K. 2013. Micrometeorite Flux on Earth during the Last ~50,000 Years. *Journal of Geophysical Research: Planets* 118: 2381–99. https://doi.org/10.1002/2013JE004460.

Rochette, P., Folco, L., Suavet, C., van Ginneken, M., Gattacceca, J., Perchiazzi, N., Braucher, R., and Harvey, R. P. 2008. Micrometeorites from the Transantarctic Mountains. *Proceedings of the National Academy of Sciences of the United States of America* 105: 18206–11. https://doi.org/10.1073/pnas.080604910.

Rojas, J., Duprat, J., Engrand, C., Dartois, E., Delauche, L., Godard, M., Gounelle, M., Carrillo-Sánchez, J. D., Pokorný, P., and Plane, J. M. C. 2021. The Micrometeorite Flux at Dome C (Antarctica), Monitoring the Accretion of Extraterrestrial Dust on Earth. *Earth and Planetary Science Letters* 560: 116794. https://doi.org/10.1016/j.epsl.2021.116794.

Rudraswami, N. G., Fernandes, D., Naik, A., Prasad, M. S., Carrillo, S. J., Plane, J., Wuhu, F., and Taylor, S. 2018. Selective Disparity of Ordinary Chondritic Precursors in Micrometeorite Flux. *Astrophysical Journal Supplement Series* 853: 38. https://doi.org/10.3847/1538-4357/aaa5f7.

Rudraswami, N. G., Genge, M. J., Marrocchi, Y., Villeneuve, J., and Taylor, S. 2020. The Oxygen Isotope Compositions of Large Numbers of Small Cosmic Spherules: Implications for their Sources and the Isotopic Composition of the Upper Atmosphere. *Journal of Geophysical Research: Planets* 125: e2020JE006414. https://doi.org/10.1029/2020JE006414.

Rudraswami, N. G., Pandey, M., Fernandes, D., Carrillo-Sánchez, J. D., Feng, W., Plane, J. M. C., and Singh, V. P. 2022. Oxygen Ablation during Atmospheric Entry: Its Influence on the Isotopic Composition of Micrometeorites. *Astrophysical Journal* 940: 25. https://doi.org/10.3847/1538-4357/ac9059.

Rudraswami, N. G., Parashar, K., and Prasad, M. S. 2011. Micrometer- and Nanometer-Sized Platinum Group Nuggets in Micrometeorites from Deep-Sea Sediments of the Indian Ocean. *Meteoritics & Planetary Science* 46: 470–491. https://doi.org/10.1111/j.1945-5100.2011.01169.x.

Rudraswami, N. G., Prasad, M. S., Babu, E. V. S. S. K., and Vijaya Kumar, T. 2016. Major and Trace Element Geochemistry of S-Type Cosmic Spherules. *Meteoritics & Planetary Science* 51: 718–742. https://doi.org/10.1111/maps.12618.

Rudraswami, N. G., Prasad, M. S., Dey, S., Fernandes, D., Plane, J. M. C., Feng, W., Taylor, S., and Carrillo-Sánchez, J. D. 2016. Relict Olivines in Micrometeorites: Precursor and Interactions in the Earth's Atmosphere. *Astrophysical Journal* 831: 197. https://doi.org/10.3847/0004-637X/831/2/197.

Rudraswami, N. G., Prasad, M. S., Nagashima, K., and Jones, R. H. 2015. Oxygen Isotopic Composition of Relict Olivine Grains in Cosmic Spherules: Links to Chondrules from Carbonaceous Chondrites. *Geochimica et Cosmochimica Acta* 164: 53–70. https://doi.org/10.1016/j.gca.2015.05.004.

Rudraswami, N. G., Suttle, M. D., Marrocchi, Y., Taylor, S., and Villeneuve, J. 2022. In-Situ O-Isotope Analysis of Relict Spinel and Forsterite in Small (<200 μm) Antarctic Micrometeorites—Samples of Chondrules & CAIs from Carbonaceous Chondrites. *Geochimica et Cosmochimica Acta* 325: 1–24. https://doi.org/10.1016/j.gca.2022.03.015.

Rudraswami, N. G., Ushikubo, T., Nakashima, D., and Kita, N. T. 2011. Oxygen Isotope Systematics of Chondrules in the Allende CV3 Chondrite: High Precision Ion Microprobe Studies. *Geochimica et Cosmochimica Acta* 75: 7596–7611. https://doi.org/10.1016/j.gca.2011.09.035.

Sheng, Y. J., Hutcheon, I. D., and Wasserburg, G. J. 1991. Origin of Plagioclase-Olivine Inclusions in Carbonaceous Chondrites. *Geochimica et Cosmochimica Acta* 55: 581–599. https://doi.org/10.1016/0016-7037(91)90014-V.

Soens, B., Chernonozhkin, S. M., de Vega, C. G., Vanhaecke, F., van Ginneken, M., Claeys, P., and Goderis, S. 2022. Characterization of Achondritic Cosmic Spherules from the Widerøefjellet Micrometeorite Collection (Sør Rondane Mountains, East Antarctica). *Geochimica et Cosmochimica Acta* 325: 106–128. https://doi.org/10.1016/j.gca.2019.11.016.

Soens, B., Suttle, M. D., Maeda, R., Vanhaecke, F., Yamaguchi, A., van Ginneken, M., Debaille, V., Claeys, P., and Goderis, S. 2020. Evidence for the Presence of Chondrule- and CAI-Derived Material in an Isotopically Anomalous Antarctic Micrometeorite. *Meteoritics & Planetary Science* 55: 2703–26. https://doi.org/10.1111/maps.13599.

Suavet, C., Alexandre, A., Franchi, I. A., Gattacceca, J., Sonzogni, C., Greenwood, R. C., Folco, L., and Rochette, P. 2010. Identification of the Parent Bodies of Micrometeorites with High-Precision Oxygen Isotope Ratios. *Earth and Planetary Science Letters* 293: 313–320. https://doi.org/10.1016/j.epsl.2010.02.046.

Suavet, C., Cordier, C., Rochette, P., Folco, L., Gattacceca, J., Sonzogni, C., and Damphoffer, D. 2011. Ordinary Chondrite-Related Giant (>800 µm) Cosmic Spherules from the Transantarctic Mountains, Antarctica. *Geochimica et Cosmochimica Acta* 75: 6200–6210. https://doi.org/10.1016/j.gca.2011.07.034.

Suttle, M. D., Dionnet, Z., Franchi, I. A., Folco, L., Gibson, J., Greenwood, R. C., Rotundi, A., King, A., and Russell, S. S. 2020. Isotopic and Textural Analysis of Giant Unmelted Micrometeorites—Identification of New Material from Intensely Altered ^{16}O-Poor Water-Rich Asteroids. *Earth and Planetary Science Letters* 546: 116444. https://doi.org/10.1016/j.epsl.2020.116444.

Suttle, M. D., and Folco, L. 2020. The Extraterrestrial Dust Flux: Size Distribution and Mass Contribution Estimates Inferred from the Transantarctic Mountains (TAM) Micrometeorite Collection. *Journal of Geophysical Research: Planets* 125: e2019JE006241. https://doi.org/10.1029/2019JE006241.

Suttle, M. D., Folco, L., Dionnet, Z., van Ginneken, M., Di Rocco, T., Pack, A., Scheel, M., and Rotundi, A. 2022. Isotopically Heavy Micrometeorites—Fragments of CY Chondrite or a New Hydrous Parent Body? *Journal of Geophysical Research: Planets* 127: e2021JE007154. https://doi.org/10.1029/2021JE007154.

Suttle, M. D., Genge, M. J., Folco, L., and Russell, S. S. 2017. The Thermal Decomposition of Fine-Grained Micrometeorites, Observations from Mid-IR Spectroscopy. *Geochimica et Cosmochimica Acta* 206: 112–136. https://doi.org/10.1016/j.gca.2017.03.002.

Suttle, M. D., Greshake, A., King, A. J., Schofield, P. F., Tomkins, A., and Russell, S. S. 2021. The Alteration History of the CY Chondrites, Investigated through Analysis of a New Member: Dhofar 1988. *Geochimica et Cosmochimica Acta* 295: 286–309. https://doi.org/10.1016/j.gca.2020.11.008.

Suttle, M. D., Hasse, T., and Hecht, L. 2021. Evaluating Urban Micrometeorites as a Research Resource: A Large Population Collected from a Single Rooftop. *Meteoritics & Planetary Science* 56: 1531–55. https://doi.org/10.1111/maps.13712.

Taylor, S., Alexander, C. M. O'D., Delaney, J. S., Ma, P., Herzog, G. F., and Engrand, C. 2005. Isotopic Fractionation of Iron, Potassium, and Oxygen in Stony Cosmic Spherules: Implications for Heating Histories and Sources. *Geochimica et Cosmochimica Acta* 69: 2647–62. https://doi.org/10.1016/j.gca.2004.11.027.

Taylor, S., Herzog, G. F., and Delaney, J. S. 2007. Crumbs from the Crust of Vesta: Achondritic Cosmic Spherules from the South Pole Water Well. *Meteoritics & Planetary Science* 42: 223–233. https://doi.org/10.1111/j.1945-5100.2007.tb00229.x.

Taylor, S., Lever, J. H., and Harvey, R. P. 1998. Accretion Rate of Cosmic Spherules Measured at the South Pole. *Nature* 392: 899–903. https://doi.org/10.1038/31894.

Taylor, S., Lever, J. H., and Harvey, R. P. 2000. Numbers, Types, and Compositions of an Unbiased Collection of Cosmic Spherules. *Meteoritics & Planetary Science* 35: 651–666. https://doi.org/10.1111/j.1945-5100.2000.tb01450.x.

Taylor, S., Matrajt, G., and Guan, Y. 2011. Fine-Grained Precursors Dominate the Micrometeorite Flux. *Meteoritics & Planetary Science* 47: 550–564. https://doi.org/10.1111/j.1945-5100.2011.01292.x.

Taylor, S., Messenger, S., and Folco, L. 2016. Cosmic Dust: Finding a Needle in a Haystack. *Elements* 12: 171–76. https://doi.org/10.2113/gselements.12.3.171.

Tenner, T. J., Ushikubo, T., Kurahashi, E., Kita, N. T., and Nagahara, H. 2013. Oxygen Isotope Systematics of Chondrule Phenocrysts from the CO3.0 Chondrite Yamato 81020: Evidence for Two Distinct Oxygen Isotope Reservoirs. *Geochimica et Cosmochimica Acta* 102: 226–245. https://doi.org/10.1016/j.gca.2012.10.034.

Thiemens, M. H., Jackson, T., Zipf, E. C., Erdman, P. W., and van Egmond, C. 1995. Carbon Dioxide and Oxygen Isotope Anomalies in the Mesosphere and Stratosphere. *Science* 270: 969–972. https://doi.org/10.1126/science.270.5238.969.

Toppani, A., Libourel, G., Engrand, C., and Maurette, M. 2001. Experimental Simulation of Atmospheric Entry of Micrometeorites. *Meteoritics & Planetary Science* 36: 1377–96. https://doi.org/10.1111/j.1945-5100.2001.tb01831.x.

Ushikubo, T., Kimura, M., Kita, N. T., and Valley, J. W. 2012. Primordial Oxygen Isotope Reservoirs of the Solar Nebula Recorded in Chondrules in Acfer 094 Carbonaceous Chondrite. *Geochimica et Cosmochimica Acta* 90: 242–264. https://doi.org/10.1016/j.gca.2012.05.010.

van Ginneken, M., Gattacceca, J., Rochette, P., Sonzogni, C., Alexandre, A., Vidal, V., and Genge, M. J. 2017. The Parent Body Controls on Cosmic Spherule Texture: Evidence from the Oxygen Isotopic Compositions of Large Micrometeorites. *Geochimica et Cosmochimica Acta* 212: 196–210. https://doi.org/10.1016/j.gca.2017.05.008.

van Ginneken, M., Genge, M. J., Folco, L., and Harvey, R. P. 2016. The Weathering of Micrometeorites from the Transantarctic Mountains. *Geochimica et Cosmochimica Acta* 179: 1–31. https://doi.org/10.1016/j.gca.2015.11.045.

van Maldeghem, F., van Ginneken, M., Soens, B., Kaufmann, F., Lampe, S., Krämer, R. L., Hecht, L., Claeys, P., and Goderis, S. 2023. Geochemical Characterization of Scoriaceous and Unmelted Micrometeorites from the Sør Rondane Mountains, East Antarctica: Links to Chondritic Parent Bodies and the Effects of Alteration. *Geochimica et*

Cosmochimica Acta 354: 88–108. https://doi.org/10.1016/j.gca.2023.06.002.

Wang, J., Davis, A. M., Clayton, R. N., Mayeda, T. K., and Hashimoto, A. 2001. Chemical and Isotopic Fractionation during the Evaporation of the FeO-MgO-SiO$_2$-CaO-Al$_2$O$_3$-TiO$_2$ Rare Earth Element Melt System. *Geochimica et Cosmochimica Acta* 65: 479–494. https://doi.org/10.1016/S0016-7037(00)00529-9.

Wasserburg, G. J., Sanz, H. G., and Bence, A. E. 1968. Potassium-Feldspar Phenocrysts in the Surface of Colomera, and Iron Meteorite. *Science* 161: 684–87. https://doi.org/10.1126/science.161.3842.684.

Yada, T., and Kojima, H. 2000. The Collection of Micrometeorites in the Yamato Meteorite Ice Field of Antarctica in 1998. *Antarctic Meteorite Research* 13: 9.

Yada, T., Nakamura, T., Noguchi, T., Matsumoto, N., Kusakabe, M., Hiyagon, H., Ushikubo, T., Sugiura, N., Kojima, H., and Takaoka, N. 2005. Oxygen Isotopic and Chemical Compositions of Cosmic Spherules Collected from the Antarctic Ice Sheet: Implications for their Precursor Materials. *Geochimica et Cosmochimica Acta* 69: 5789–5804. https://doi.org/10.1016/j.gca.2005.08.002.

Yada, T., Nakamura, T., Takaoka, N., Noguchi, T., Terada, K., Yano, H., Nakazawa, T., and Kojima, H. 2004. The Global Accretion Rate of Extraterrestrial Materials in the Last Glacial Period Estimated from the Abundance of Micrometeorites in Antarctic Glacier Ice. *Earth, Planets and Space* 56: 67–79. https://doi.org/10.1186/BF03352491.

Young, E. D. 2001. The Hydrology of Carbonaceous Chondrite Parent Bodies and the Evolution of Planet Progenitors. *Philosophical Transactions of the Royal Society of London. Series A: Mathematical, Physical and Engineering Sciences* 359: 2095–2110. https://doi.org/10.1098/rsta.2001.0900.

Young, E. D., Galy, A., and Nagahara, H. 2002. Kinetic and Equilibrium Mass-Dependent Isotope Fractionation Laws in Nature and their Geochemical and Cosmochemical Significance. *Geochimica et Cosmochimica Acta* 66: 1095–1104. https://doi.org/10.1016/S0016-7037(01)00832-8.

Zolensky, M. E., Krot, A. N., and Benedix, G. 2008. Record of Low-Temperature Alteration in Asteroids. *Reviews in Mineralogy and Geochemistry* 68: 429–462. https://doi.org/10.2138/rmg.2008.68.15.

SUPPORTING INFORMATION

Additional supporting information may be found in the online version of this article.

Table S1. In situ measurements of the oxygen isotopic composition of different types of cosmic spherules.

19455100, 0, Downloaded from https://onlinelibrary.wiley.com/doi/10.1111/maps.14145 by Test, Wiley Online Library on [09/02/2024]. See the Terms and Conditions (https://onlinelibrary.wiley.com/terms-and-conditions) on Wiley Online Library for rules of use; OA articles are governed by the applicable Creative Commons License